SELF-CALIBRATION TECHNIQUE FOR TRANSMITTED WAVEFRO`NT
MEASURMENTS OF MICRO-OPTICS


by


Brent C. Bergner


A thesis submitted to the faculty of the
University of North Carolina at Charlotte
in partial fulfillment of the requirements for
the degree of Master of Science in
Optical Science and Engineering

Charlotte

2004


Approved By:


_____
Dr. Angela D. Davies


_____
Dr. Thomas J. Suleski


_____
Dr. Robert J. Hocken

ABSTRACT

BRENT C. BERGNER. Self-Calibration Technique for Transmitted Wavefront Measurements of Micro-Optics. (Under the direction of DR. ANGELA DAVIES)


Micro-optic components and subsystems are becoming increasingly important in optical sensors, communications, data storage, and many other applications. In order to adequately predict the performance of the final system, it is important to understand how the optical elements affect the wavefront as it is transmitted through the system. The wavefront can be measured using interferometric means; however, both random and systematic errors contribute to the uncertainty of the measurement. If an artifact is used to calibrate the system it must itself be traceable to some external standard. Self-calibration techniques exploit symmetries of the measurement to separate the systematic errors of the instrument from the errors in the test piece. We have developed a self calibration technique to determine the systematic bias in a Mach-Zehnder interferometer. If the transmitted wavefront of a ball lens is measured in a number of random orientations and the measurements are averaged, the only remaining deviations from a perfect wavefront will be spherical aberration contributions from the ball lens and the systematic errors of the interferometer. If the radius, aperture, and focal length of the ball lens are known, the spherical aberration contributions can be calculated and subtracted, leaving only the systematic errors of the interferometer. This thesis describes the development of an interferometer that can be used to measure micro-optics in either a Mach-Zehnder or Twyman-Green configuration. It also develops the theory behind the technique used to calibrate for transmitted wavefront and describes the calibration of the interferometer in the Mach-Zehnder configuration.

# DEDICATION

I would like to dedicate this thesis to my parents, Charles and Alice Bergner, who have worked hard and always given me support and encouragement in all of my endeavors, and to my brother, Brian Bergner, who was serving his country in Iraq as I worked on this project.

ACKNOWLEDGEMENTS

I would like to acknowledge the other members of the research team: Neil Gardner, Kate Medicus, Devendra Karodkar, Ayman Samara, and Solomon Gugsa who contributed significantly to the design and construction of the interferometer. I would also like to thank Dr. Faramarz Farahi for his assistance in considering interferometer configurations, Dr. Robert Hocken for discussing uncertainty in self-calibration techniques, and Dr. Thomas Suleski for help in understanding diffraction effects from small features. I would like to thank Dr. Robert Parks and Dr. Christopher Evans for their discussions on self-calibration techniques, Dr. Horst Schreiber for clarifying important issues concerning imaging systems in interferometers, and Jeremy Huddleston for assistance with developing the ZEMAX® models used to calculate the spherical aberration contribution of the ball lens. I would also like to express my appreciation to Barbara Kremenliev for her help and encouragement throughout the project. . Finally, I would like to acknowledge the many discussions with, and encouragement, and advice from my advisor, Dr. Angela Davies.

TABLE OF CONTENTS

CHAPTER 1: INTRODUCTION

Micro-optic components and subsystems are becoming increasingly important in optical sensors, communications, data storage, and many other diverse applications. In general, the term micro-optics is used to describe optical elements and systems with clear apertures from 0.1 to 1 millimeter.[1] These may include diffractive elements, gradient index (GRIN) lenses, or surface relief refractive structures. While some of the techniques developed in this thesis may also be applied to the evaluation of guided wave optics they are not specifically considered. It is also assumed that the elements and systems are symmetric about the optical axis.

1.1 Applications for Micro-Optics

Micro-optics have found a wide range of applications. In order to understand the requirements of the measurement system it is important to understand the applications and tolerances involved. This is not an exhaustive survey, but an attempt to define the problem and design a measurement system that is adequate for general purpose use.

Micro-optic elements can be integrated into compact systems. In addition to free space integration, for example using a silicon optical bench, micro-optics can be integrated in a planar or stacked manner[2] as shown in figure 1.1. For example, micro-optic systems can be used for optical interconnects, optical processing, and compact instrumentation such as micro-interferometers[3]. A critical parameter for such systems is the space bandwidth product (SBP), the ratio of the image area to the image spot size.[4]

The higher the SBP, the more information can be transmitted through the system. The image spot size is related to the wavelength, the aperture size, and the wavefront aberrations of the system.[5]
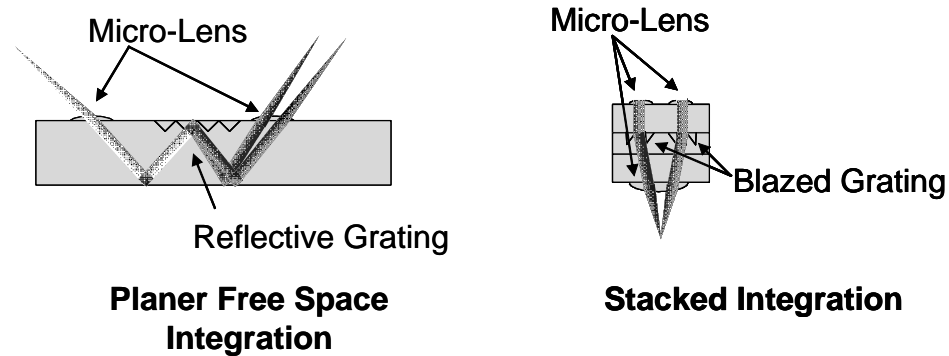


**Figure 1.1  Examples of micro-optic systems created with planar integrated free space micro-optics and stacked micro-optics (adapted from J. Jahns, "Planer integrated free space optics" in  *Micro-optics*, H.P. Herzig ed. ).[2]**

An application that has gained significant attention involves coupling light between single mode optical fibers (see figure 1.2). This can be used for integration of free space optical components such as filters, isolators and optical switches into fiber optic communication systems. Wagner and Tomlinson investigated the effects of wavefront aberrations on the coupling efficiency between single mode optical fibers.[6] They found that a peak-to-valley transmitted wavefront error of one fifth wave in the imaging system would cause a 0.9 dB loss.
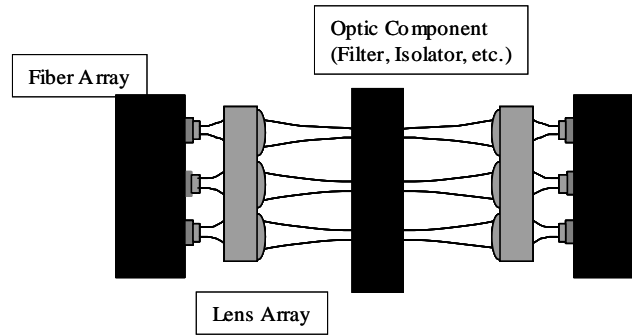
**Figure 1.2  Arrays of refractive micro-lenses are used to couple optical signals between single mode fibers in passive fiber optic components.**

Optical storage devices such as CDs and DVDs have replaced magnetic storage media in many applications.[7]  Figure 1.3 shows a conceptual representation of an optical pick up head using stacked micro-optics.  The optical performance of each element in the system is critical to obtaining the optimal storage density.
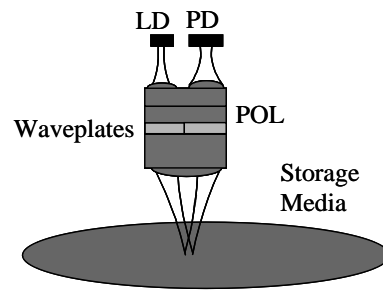


**Figure 1.3  Stacked planar optics are used to detect polarization changes caused by the storage media.  The transmitted wavefronts of each of the micro-lenses, as well as the entire assembly, are important to the performance of the system.**

In addition, as with conventional optical systems, alignment of the micro-optical elements will affect the final system performance.  An advantage of micro-optics is that it is often possible and even convenient to fabricate multiple elements on a single substrate.  Many systems can then be aligned in a parallel manner by properly aligning the substrates.  Ideally, these alignments would be achieved passively using mechanical features integrated with the optical elements; however, in many cases the required

alignment tolerances can only be achieved using active alignment. This might involve visually aligning fiducial marks or monitoring some functional parameter of the system to provide the feedback. In many cases, the aberrations of the transmitted wavefront provide an excellent functional measure of the system performance.

1.2 Fabrication of Micro-Optics

Micro-optic elements can be fabricated using a variety of methods including ion exchange, lithography, diamond machining, and various replication techniques. For example, ion exchange can be used to modify the local index of refraction of a substrate.[1] The change in index will change the phase of a wavefront passing through the substrate. As illustrated in figure 1.4, the index change can be controlled to create a gradient index (GRIN) region that acts as a lens.[4]
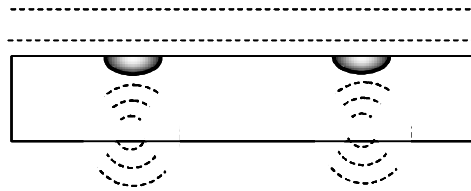


**Figure 1.4  Ion exchange is used to modify the local index of refraction of the substrate creating gradient index (GRIN) lenses (from M. Testorf and J. Jahns, "Imaging properties of planar integrated micro-optics").[4]**

The phase of the wavefront can also be controlled using diffraction. As shown in figure 1.5, binary diffractive elements are commonly fabricated using techniques similar to those used for micro-electronics.[8] The substrate is spin coated with a photo-sensitive polymer and selectively exposed to ultra-violet light. A pattern is left on the substrate when the resist is developed. The resist pattern can itself act a phase grating or it can be transferred into the substrate by chemical or plasma etching. A better

approximation of the ideal phase profile can be built up by repeating the process to add

phase levels, or continuous relief structures can be created using grayscale lithography.
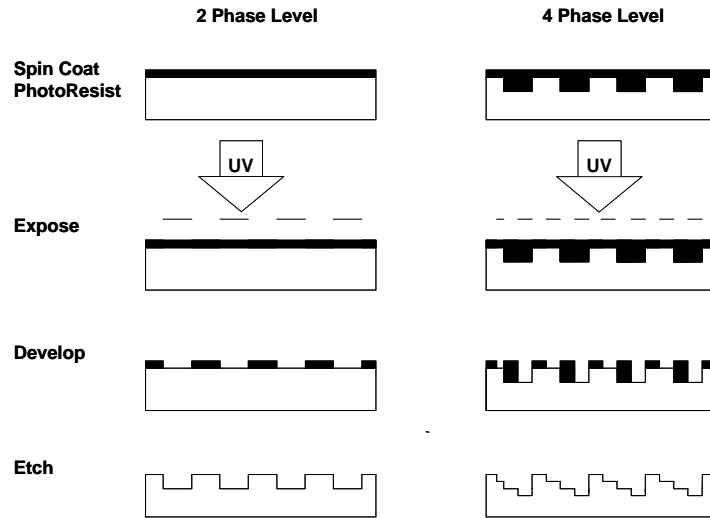


**Figure 1.5  Diffractive micro-optic elements can be fabricated using lithographic processes similar to those used for micro-electronics (adapted from D.C.  O'Shea, T.J. Suleski, A. D. Kathman, and D.W. Prather,** *Diffractive Optics: Design, Fabrication, and Test*).[8]

Surface relief refractive micro-lenses (shown in figure 1.6) can be fabricated

using grayscale lithography or reflow techniques.[9]  In reflow techniques the exposed and

developed resist pattern is heated just beyond its glass transition temperature and surface

tension causes the resist to form a hemisphere.  Again, the resist can act as a refractive

lens or the pattern can be transferred into the substrate.



**Figure 1.6    Surface relief refractive micro-lenses can be fabricated using a reflow technique. (Adapted from G. R. Brady,** *Design and Fabrication of Microlenses*).[9]

Single point diamond turning has been used extensively to directly machine

micro-optics.[10]  Using precision machine tools and single point diamond cutting tools

optical quality surface relief structures can be directly machined in non-ferrous metals,

polymers, and certain crystals.  For rotationally symmetric elements the substrate is attached to the spindle of a lathe and a single point diamond tool is used to profile the surface as shown in figure 1.7.
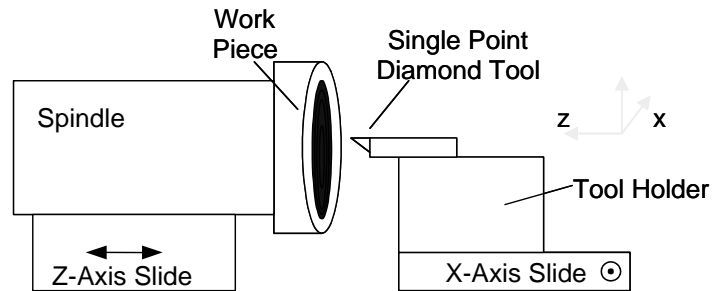


**Figure 1.7 The substrate is attached to the spindle of a lathe to fabricate rotationally symmetric elements and a single point diamond tool is used to profile the surface.**

Finally, surface relief micro-structures can be replicated in polymers, sol-gels, or glass by casting, embossing, compression molding, or a variety of other techniques.   The mold can be directly produced with methods such as those already mentioned, or a more robust copy of the original master can be made using electrolytic nickel platting.[11]

1.3 Testing of Micro-Optics

Systems integrators, designers, and manufactures are interested in a variety of dimensional and optical properties of micro-optics.   Some critical parameters are illustrated in figure 1.8.  For example, to evaluate the fitness of an as-manufactured optic to perform adequately in a particular application, the system integrator would like to measure parameters such as the transmitted wavefront quality (TWF), the modulation transfer function (MTF), the point spread function (PSF), and the back focal length (BFL).[12]  Along with other dimensional and optical properties such as clear aperture (CA), fill factor, and optical efficiency, these can be referred to as *functional criteria*.

Manufacturers are interested in more detailed information about the lens shape such as radius of curvature (ROC) and form errors, which can be directly related to the bias and stability of the process. These are can be referred to as *process-related measurements*.
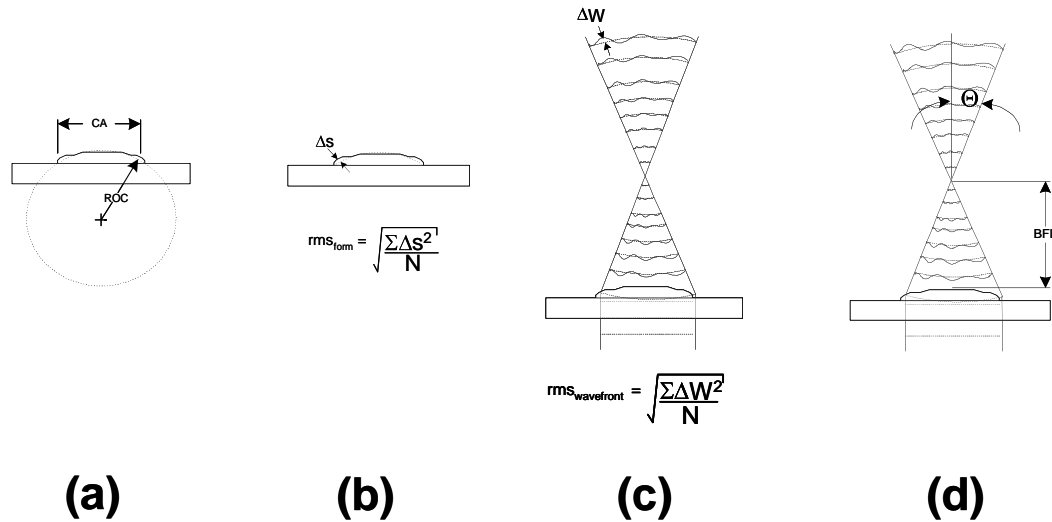


**Figure 1.8 Important characteristics of a refractive micro-lens are a) Radius of Curvature (ROC), b) Surface Form Deviations ($\Delta S$), c) Transmitted Wavefront Deviations ($\Delta W$), and d) Back Focal Length (BFL). *CA* is the clear aperture of the lens, *rms* is the root mean square value, *N* is the number of sample points used to compute the rms value, and the sine of $\Theta$ is the image side numerical aperture of the lens with an infinite conjugate.**

Form can be measured using mechanical or optical profilers, or interferometeric techniques that measure the wavefront reflected from the surface. Back focal length and radius of curvature are commonly measured using a radius slide.[13] Transmitted wavefront measurements are the primary concern of this thesis. MTF and PSF can be measured directly using a variety of techniques or they can be calculated from the transmitted wavefront.[14]

Measurements of micro-optics present unique challenges compared to equivalent measurements of optics with clear apertures on the order of tens of millimeters or larger.[15] As discussed in more detail in section 2.2, diffraction effects and retrace errors

can become significant as the size of the features of interest approach the order of hundreds of micro-meters. Due to diffraction effects and retrace errors, the TWF of micro-optics should be measured in a single pass configuration. This limits the choice of interferometer configurations to those that have a significant non-common path. Since the ROC (or BFL) of the lens tends to be small compared to the focal length of the objective used to create a reference wavefront, imaging the surface or aperture of the lens onto the image sensor can also present a challenge. This is discussed in Section 3.2. Finally, since the ROC and BFL are usually in the order of a millimeter or less, stage error motions in the radius slide can contribute significant uncertainty to the measurements of these quantities.

When measuring micro-optics, wavefront errors in the interferometer can add a significant bias to transmitted wavefront measurements. As discussed in section 2.3, a "well-corrected" reference objective is assumed throughout the literature. This thesis develops and demonstrates a technique to account for the bias in the interferometer including aberrations in the reference objective. We propose to measure the transmitted wavefront of a ball lens in a number of random orientations and then average the measurements. The only remaining deviations of the average from a perfect wavefront will be due to spherical aberration contributions from the ball lens and the systematic errors of the interferometer. If the radius, aperture, and focal length of the ball lens are known, the spherical aberration contributions can be calculated and subtracted, leaving only the bias in the wavefront measurement due to the interferometer.

CHAPTER 2:  BACKGROUND

2.1.   Self-Calibration Techniques

Every measurement consists of a combination of the value being measured (the *measurand*), systematic bias, and random noise.  The systematic bias should be reduced as much as possible, however some residual will always remain.  If the residual can be estimated, it can then be subtracted from the final measurement to obtain a better estimate of the measurand.  One method of estimating the residual is to measure a known artifact.  However, in many cases, artifacts either have uncertainties comparable to the required measurement uncertainty, or they do not exist.  This is common in the measurement of micro-optics.  In these cases, it is necessary to use "self-calibration" techniques to separate instrument bias from the errors due to the part under test.[16]

In general, self-calibration techniques rely on symmetry to eliminate the contribution of the artifact to the measurement.[17]   For example, a straight edge and indicator are used to measure the straightness of a slide.  In figure 2.1a, the measured deviation, $I_1(x)$, will be due to both the straightness errors of the slide, $M(x)$, and any deviation of the straightedge, $S(x)$, so that

$$I_1(x) = M(x) + S(x)$$

**(2.1)**
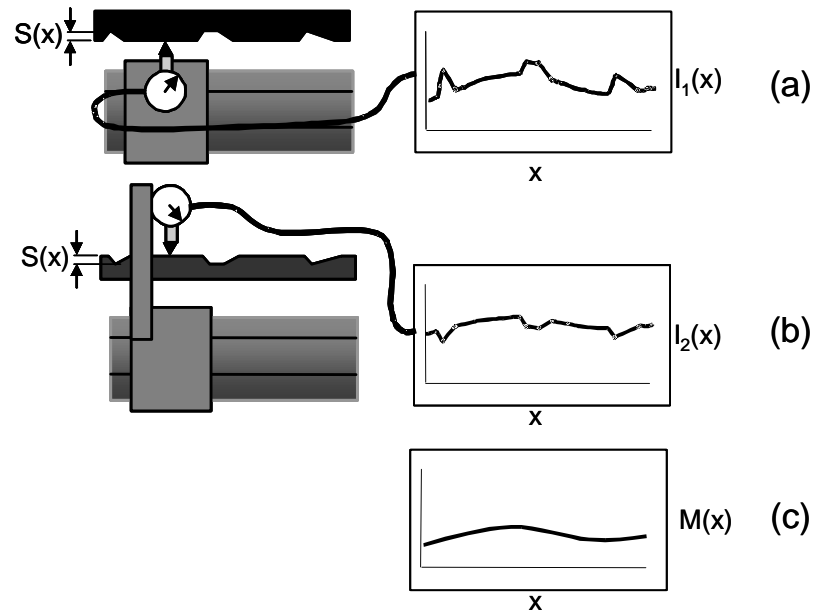
**Figure 2.1 Straight edge reversal as an example of a self-calibration technique using reversal (from C.J. Evans, R.J. Hocken, and W.T. Estler, "Self-calibration: reversal, redundancy, error separation, and "absolute testing").[16]**

However, if a second measurement, $I_2(x)$, in figure 2.1b is taken with the straight edge flipped about an axis parallel to the axis of motion of the stage, then the sign of the deviations of the straightedge will be reversed but the deviation due to the straightness error will not change sign, so that

$$I_2(x) = M(x) - S(x)$$.

**(2.2)**

By averaging these two measurements, the effect of the deviations of the straightedge will be eliminated leaving only the deviations due to the straightness errors of the slide, as shown in figure 2.1c.

$$M(x) = [I_1(x) + I_2(x)]/2$$.

**(2.3)**

This type of self calibration technique is often referred to as a *reversal* since it relies on reversing the bias in the measurement due to an imperfect artifact.
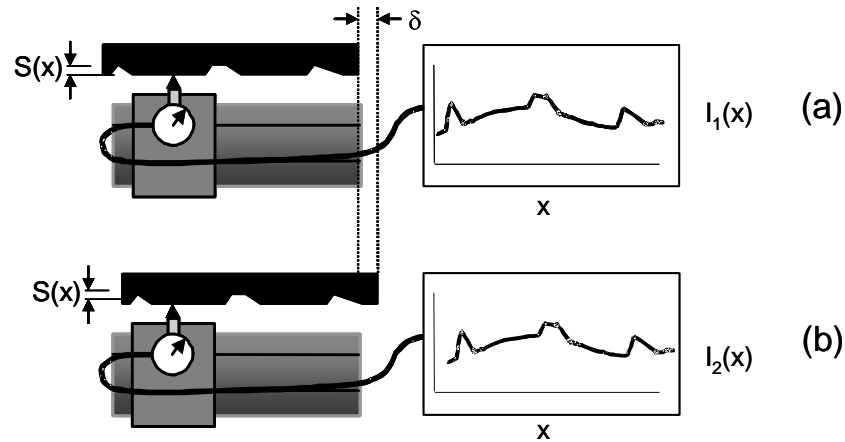
**Figure 2.2 Setup for measuring straightness using offset (from C.J. Evans, R.J. Hocken, and W.T. Estler, "Self-calibration: reversal, redundancy, error separation, and "absolute testing").[16]**

The bias due to an imperfect artifact can also be removed by offsetting the artifact, as shown in figure 2.2.  The original measurement in figure 2.2a will again be

$$I_1(x) = M(x) + S(x),$$

**(2.4)**

and, if the artifact is offset by a distance ($\delta$) along the direction of travel of the stage (as shown in figure 2.2b), the offset measurement will be

$$I_2(x) = M(x) + S(x+\delta).$$

**(2.5)**

Subtracting the two measurements and dividing by the offset gives the derivative of deviation due to the errors in the straightedge,

$$\frac{I_2(x) - I_1(x)}{(x+\delta) - x} = \frac{S(x+\delta) - S(x)}{\delta}.$$

**(2.6)**

Equation 2.6 can be integrated to retrieve the deviations of the straightedge $S(x)$. This value can then be subtracted from either equation 2.4 or equation 2.5 to find the deviations due to the straightness errors of the slide.

Another important concept in self-calibration is closure, which relies on some physical constraint to estimate the bias of the artifact. For example, the divisions of a complete circle must add to 360 degrees. This technique has been used to measure the external angles of a polygonal mirror.[18]

In this setup, two autocollimators are set with an angular separation as shown in figure 2.3, where $N$ is the number of facets of the polygon and $\Delta$ is the difference between the actual angle between the autocollimators (in degrees) and 360/$N$.
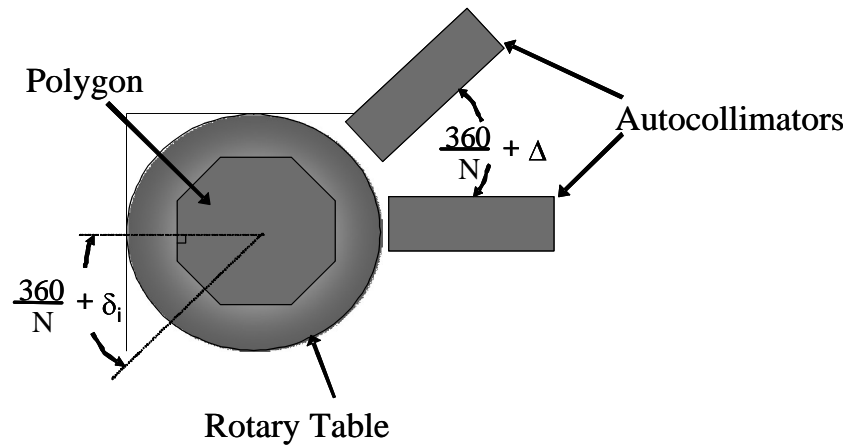


**Figure 2.3 Setup for determining the angles of a polygon using closure.**

For each pair of adjacent facets the difference in the error signals from the two autocollimators will be

$$\varepsilon = \delta - \Delta ,$$

**(2.7)**

where δ is the difference between the actual angle between the normals and the ideal angle if all of the polygon angles were equal. Notice that it is not necessary that $\delta$ be small. Since the angles between the normals must form a complete circle,

$$\sum_{i=1}^{N}\left(\frac{360}{N}+\delta_i\right) = N\frac{360}{N}+\sum_{i=1}^{N}\delta_i = 360 .$$

(2.8)

Therefore,

$$\sum_{i=1}^{N}\delta_i = 0 .$$

(2.9)

Consequently,

$$\frac{\sum_{i=1}^{N}\varepsilon_i}{N} = \frac{\sum_{i=1}^{N}(\delta_i-\Delta)}{N} = -\Delta$$

(2.10)

and the angle between the autocollimators ($\alpha$) is

$$\alpha = \frac{360}{N} - \frac{\sum_{i=1}^{N}\varepsilon_i}{N} .$$

(2.11)

This appears to be equivalent to the reversal technique, but more than two measurements are needed to complete the symmetry and eliminate the artifact bias. Now that the actual angle between the autocollimators is known, this value can be used to compute the angle between the $k^{th}$ set of facet normals ($\beta_k$),

$$\beta_k = \frac{360}{N} + \varepsilon_k + \frac{\sum_{i=1}^{N}\varepsilon_i}{N} = \frac{360}{N} + \left(\frac{N-1}{N}\right)\varepsilon_k + \frac{\sum_{i\neq1}^{N}\varepsilon_i}{N}.$$

<div align="right">(2.12)</div>

A final class of self-calibration techniques that will be discussed here involves averaging. Averaging might be considered a further extension of the techniques discussed previously. However, averaging assumes that the deviations of an artifact can be considered to be random and uncorrelated. If this is a valid assumption, then the deviations can be treated similarly to random noise.[19]

It is important to notice that in all of these techniques there is still uncertainty associated with the calibration process. It is important to consider how the data were taken and analyzed when considering the uncertainty of the bias estimate. As shown below, if the standard deviation of the measurements in the average is used to calculate the uncertainty in the bias estimate, then the contribution is the standard deviation divided by the square root of the number of measurements.

The standard equation for the propagation of uncertainty is[20]

$$u_c^{\;2}(y) = \sum_{i=1}^{N}\left(\frac{\delta f}{\delta x_i}\right)^2 u^2(x_i) + 2\sum_{i=1}^{N}\;\sum_{j=i+1}^{N}\frac{\delta f}{\delta x_i}\frac{\delta f}{\delta x_i}u(x_i,x_j)$$

<div align="right">(2.13)</div>

where $u_c(y)$ is the combined uncertainty of the measurand given by $y = f(x_1, x_2, \dots x_N)$, $u(x_i)$ is the standard uncertainty of the $i^{th}$ contribution to the result, and $(\delta f/dx_i)$ is called the *sensitivity coefficient*. The sensitivity coefficient represents the sensitivity of the value of the function to small changes in the value of $x_i$ as shown in figure 2.4.

$f(x_i)$

$x_i$
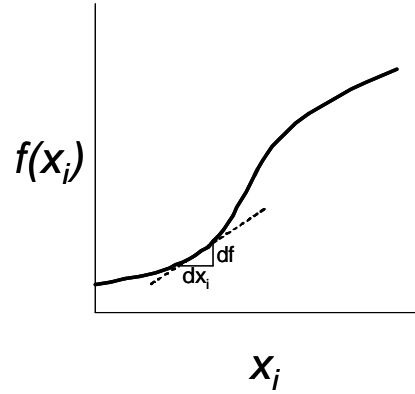
**Figure 2.4 Graphical representation of a general function *f(x_i)* demonstrating the significance of the sensitivity coefficient ($\delta f/\delta_{xi}$).**

The term $(\delta f/dx_i)\, u(x_i)$ is the first term in a Taylor series expansion of $f(x_i)$.[21] The double sum represents the effect of correlations between the contributions where $u(x_i, x_j)$ is the covariance of the $x_i$ and $x_j$ terms. The covariance can be related to the correlation between the variables by[22]

$$u(x_i, x_j) = \mathrm{cov}(x_i, x_j) = cor(x_i, x_j)u(x_i)u(x_j)$$

**(2.14)**

For example, assuming small errors and no significant correlations between $I_1(x)$ and $I_2(x)$, the combined uncertainty in the estimate of the straightness error of the slide, given by equation 2.3 is

$$u_c(M) = \sqrt{(\tfrac{1}{2})^2 u^2(I_2) + (\tfrac{1}{2})^2 u^2(I_1)}$$

**(2.15)**

If we assume that $u^2(I_1) = u^2(I_2) = u^2(I)$ then

$$u_c(M) = \frac{u(I)}{\sqrt{2}}$$

**(2.16)**

However, if the uncertainties in $I_1(x)$ and $I_2(x)$ are perfectly correlated and

$u^2(I_1) = u^2(I_2) = u^2(I)$ then

$$u_c(M) = \sqrt{(\tfrac{1}{2})^2 u^2(I) + (\tfrac{1}{2})^2 u^2(I) + 2(\tfrac{1}{2})(\tfrac{1}{2})u(I)u(I)} = u(I)$$ .

$$(2.17)$$

In general, for the case of averaging N uncorrelated values

$$u_c = \sqrt{\left(\frac{1}{N}\right)^2 u^2(x_1) + \left(\frac{1}{N}\right)^2 u^2(x_2) \ldots + \left(\frac{1}{N}\right)^2 u^2(x_N)}$$ .

$$(2.18)$$

If $u^2(x_1) = u^2(x_2) = \ldots = u^2(x_N) = u^2(x)$ then

$$u_c = \sqrt{N\left(\frac{1}{N}\right)^2 u^2(x)} = \frac{u(x)}{\sqrt{N}}$$ .

$$(2.19)$$

Self-calibration techniques are common in optical testing. Jensen[23] presented a technique for calibrating a Twyman-Green interferometer in 1973. The three-flat test[24] and N-position test[25] are further examples. Averaging randomly sampled measurements of a surface has been used to calibrate roughness measurements.[19] Measurements of random patches of a large optical flat can be averaged together to estimate systematic biases in flatness measurements, and a similar technique using sub aperture patches on a ball has been used to calibrate interferometer transmission spheres[26] and Twyman-Green interferometers used for micro-refractive lens measurements.[27]  By averaging the transmitted wavefronts from a randomly positioned ball lens we have extended the

averaging technique to transmitted wavefront measurements in a Mach-Zehnder configuration.

## 2.2. Challenges in Measuring Transmitted Wavefront of Micro-optics

A double pass interferometeric method using a Fizeau or Twyman-Green configuration is commonly used to test the transmitted wavefront of optics.[28] Some common configurations used for testing microscope objectives are shown in figure 2.5.
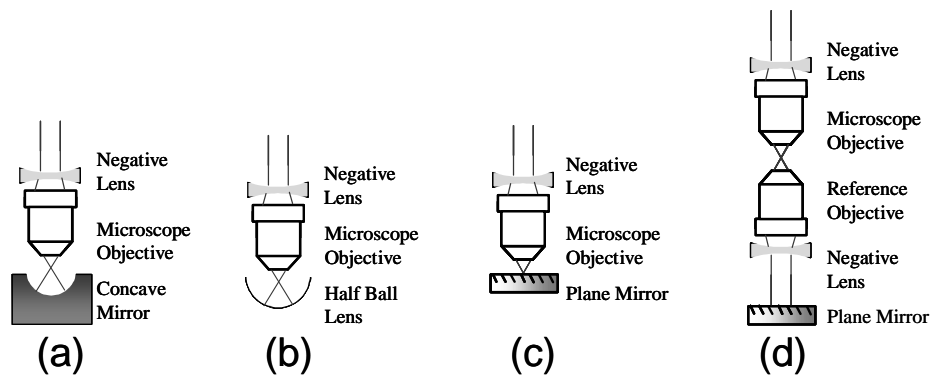


**Figure 2.5 Configurations for testing microscope objectives using a Twyman-Green Interferometer (from D. Malacara, "Twyman-Green Interferometer" in *Optical Shop Testing*, D. Malacara ed.).[28]**

Since the wavefront passes through the lens under test twice, the transmitted wavefront of the lens is often approximated as half the wavefront error measured in the double pass configuration. For this approximation to be valid, the wavefront leaving the exit pupil of the test optic must be imaged with the correct phase back onto the exit pupil of the lens under test (see figure 2.6).
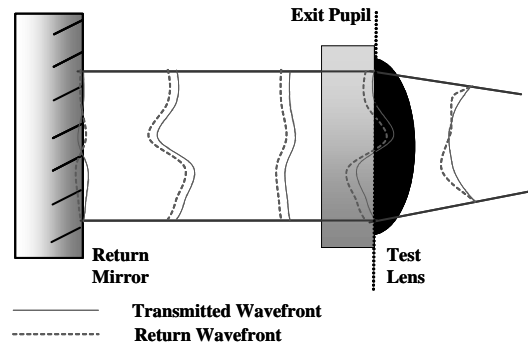
**Figure 2.6  The return wavefront must  be imaged with the correct phase back onto the exit pupil of the lens under test.**

Dyson presented a solution for imaging the wavefront back onto the exit pupil without third order Seidel aberrations for a unit magnification.[29]   The imaging system consists of a half ball lens and a concave spherical mirror as shown in figure 2.7.  The radius of the mirror ($R_2$) is related to the radius of the half ball lens ($R_1$) by

$$R_2 = R_1 \left( \frac{n}{n-1} \right)$$

(2.20)

where $n$ is the index of refraction of the half ball lens.
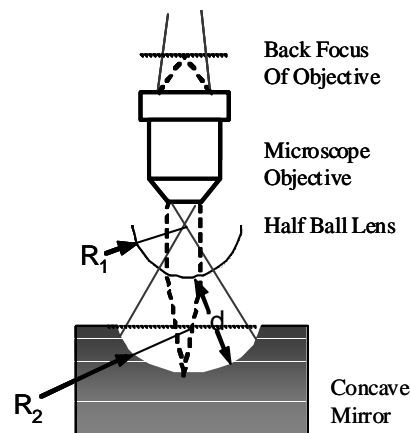


**Figure 2.7    Dyson's configuration for testing a microscope objective (from D. Malacara, "Twyman-Green Interferometer" in *Optical Shop Testing*, D. Malacara ed.).[28]**

If the center of curvature of the mirror coincides with the center of curvature of the lens, the third order Seidel aberrations of the mirror and ball lens will cancel. However, form errors, alignment, and diffraction will affect this result.

As a wavefront propagates through free space (see figure 2.8), each spatial frequency ($1/p$) of the wavefront will oscillate in phase and amplitude with a longitudinal period equal to a characteristic length ($L_F$) given by[30]

$$L_F = \frac{2p^2}{\lambda} \, .$$

**(2.21)**

For larger optics the distance from the exit pupil to the return flat is much less than this characteristic length, and diffraction affects are not significant for most applications. For example, for the spatial frequencies corresponding to the edge of an optic with a twenty-five millimeter aperture, the characteristic length is almost two-thousand meters. If the return mirror is placed within a meter of the exit pupil, then it is normally assumed that the change in the wavefront due to this diffraction will not be significant and that small changes in the position of the mirror will have little effect on the result. However, for a lens with an aperture of one half millimeter, the characteristic length is only seven-hundred and ninety millimeters. Each spatial frequency in the wavefront will have a different characteristic period. While the return optics may be aligned to correctly reproduce the phase of a single spatial frequency, there will be an significant error for nearby spatial frequencies.
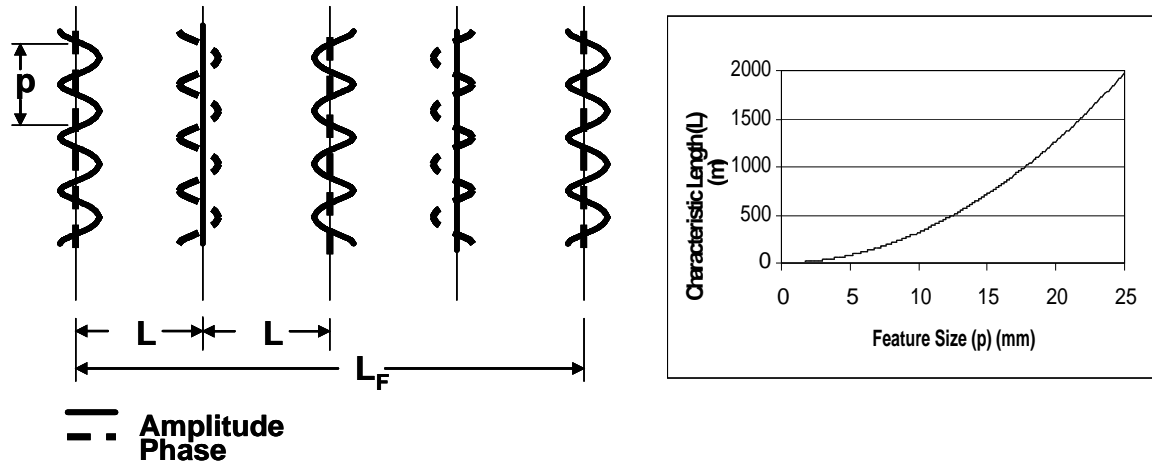
**Figure 2.8  For each spatial frequency the amplitude and phase of the wavefront changes as it propagates through free space (from M. Bray, "Stitching Interferometery Side effects and PSD").[30]**

2.3.    Techniques for Measuring  Transmitted Wavefront of Micro-Optics

Microscope objectives and similar optics can be tested with standard interferometers using the setups illustrated in figure 2.5.   However, as discussed in section 2.2, there are unique challenges to correctly measuring the transmitted wavefront of micro-optics.   Several groups have adapted both geometric and interferometeric methods for wavefront sensing to instruments specifically designed for measuring the transmitted wavefront of micro-optics.   Each system has advantages and limitations. These are summarized in table 2.1.

**Table 2.1 Summary of advantages and disadvantages of selected techniques for measuring the transmitted wavefront of micro-optics.**

| Technique | Advantages | Disadvantages | Reference |
|-----------|------------|---------------|-----------|
| Hartman Test | - Simple Setup<br>- Relatively insensitive to vibrations | - Spatial resolution is limited by the pitch of the lens array | 31 |
| Shearing Interferometery | - Lens under test is outside the interferometer<br>- Non-common path can be very short<br>- Easily reconfigured for reflection or transmission measurements | - Requires two shears in orthogonal directions to reconstruct rotationally variant wavefront | 32,33,34 |
| Double-Pass Twyman-Green | - Simple setup on commercially available interferometer | - Double pass configuration is sensitive to diffraction and retrace errors. | 35 |
| Mach-Zehnder | - Single pass interferometeric method | - Large non-common path | 9,36,37,38,39 |

The Shack-Hartmann test uses an array of lenses to sample a wavefront. Each lenslet forms a spot on an observation screen (or CCD camera). As illustrated in figure 2.9, the position of each spot depends on the local slope of the wavefront at that location of the lenslet in the array. The phase of the wavefront can be determined by integrating the slope, either using a point by point discrete integration or by fitting a polynomial to the slope and then integrating.
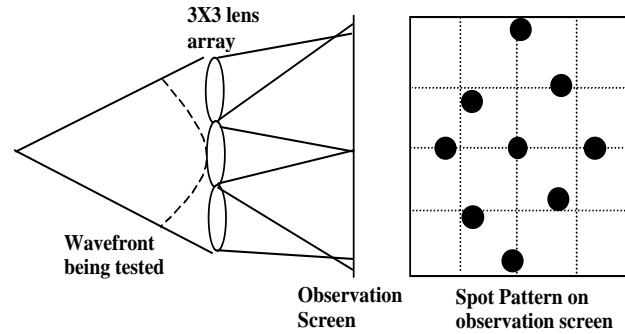
**Figure 2.9  In a Shack-Hartmann test, a lenslet array is used to sample a wavefront. The positions of the spots in on the screen depend on the slope of the wavefront at each lenslet.  In practice, there are usually several hundred, or even thousands, of lenslets in the array.**

Pulaski et al.[31]  measured the transmitted wavefront of a micro-lens using a beam expander to magnify the wavefront from the lens under test (see figure 2.10).  They calibrated the system by replacing the test lens with a precision lens that they assumed to be free from aberrations.
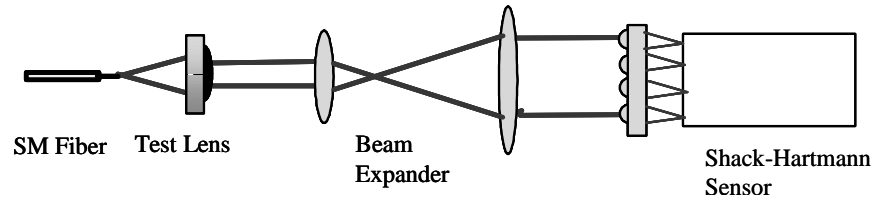


**Figure 2.10  Arrangement using a Shack-Hartmann sensor to measure a microlens.  (from Pulaski et al., "Measurment of abearations of microlenses using a Shack-Hartmann wavefront sensor").[31]**

Shearing interferometery has also been used to measure the transmitted wavefront of micro-optics.[32, 33, 34]  The wavefront being tested is split.  The two new wavefronts are spatially shifted (sheared) with respect to each other and recombined to form an interference pattern.   The resulting pattern is related to the derivative of the original wavefront in the direction of the shear.   This is similar to the offset method in self-calibration in that the measured value is the derivative of the measurand.  In order to completely reconstruct a rotationally variant wavefront it is necessary to take two

measurements with the shear in orthogonal directions. Sickinger et al.[34] used a Michelson–type shearing interferometer like the one illustrated in figure 2.11 to measure the form, focal length, and transmitted wave aberrations of micro-lenses.
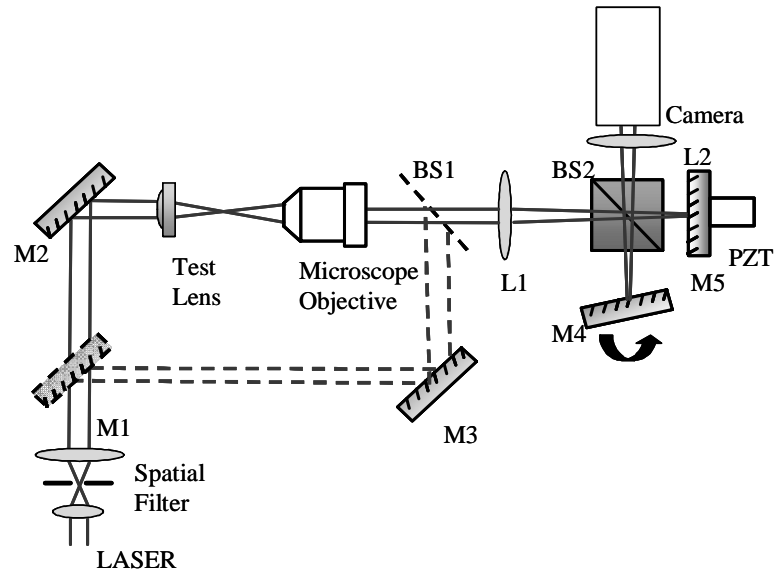


**Figure 2.11 Shearing interferometer used at the National Physics Laboratory (NPL), the United Kingdom's national measurement laboratory, to measure transmitted wavefront (from H. Sickinger et al., "Characterization of microlenses using a phase shifting shearing interferometer").[34]**

This technique has several advantages. Since the lens under test is outside the interferometer, the sources can be replaced with fiber without regard to optical path length changes in the fiber. Within the operating wavelengths of the mirrors and beam splitters, it is insensitive to wavelength. However, M4 must be tilted during the measurement to get the shear for two orthogonal directions. In addition, BS2 adds systematic spherical aberration to the wavefront, and the defocus added by phase shifting can only be ignored if L1 is slow and M5 is only moved a small distance. They also assumed that the microscope objective was diffraction limited and that it did not add significant bias.
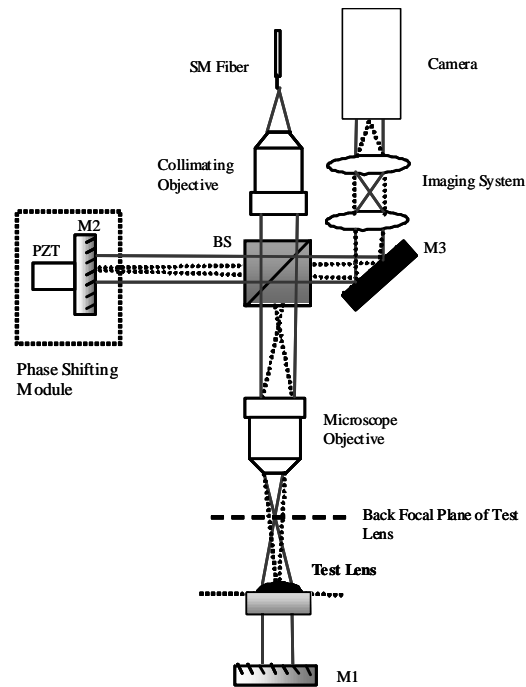
**Figure 2.12 Configuration used by Malyak et al.[35] to test the transmitted wavefront of micro-lenses. It was based on a commercial Twyman-Green interferometer.**

Malyek et al. [35] used a Twyman-Green configuration based on a commercially available interferometer to test lenses used to couple light between single mode fibers used in telecommunications applications. The setup is shown in figure 2.12. The coupling efficiency they predicted based on the transmitted wavefront measurements did not correlate well with functional tests they performed on the same lenses. Since the aperture of the lenses was on the order of a few hundred wavelengths, diffraction effects discussed in section 2.2 may have contributed to a significant error in the transmitted wavefront measurement. These effects can be eliminated when measuring the transmitted wavefront in a single pass configuration if the interferometer is focused on the exit pupil of the lens system under test.

A common method for testing the transmitted wavefront in a single pass is to use a Mach-Zehnder configuration.[9,36,37,38,39] In a Mach-Zehnder interferometer, a beam splitter divides the beam into two paths and the beams are recombined at a second beam splitter. The resultant interferogram is related to the optical path difference between the two paths. Usually, one path contains the object to be tested and the other acts as a reference. The optical path length of either path may be changed in a controlled manner to implement phase shifting techniques for analyzing the interference pattern.
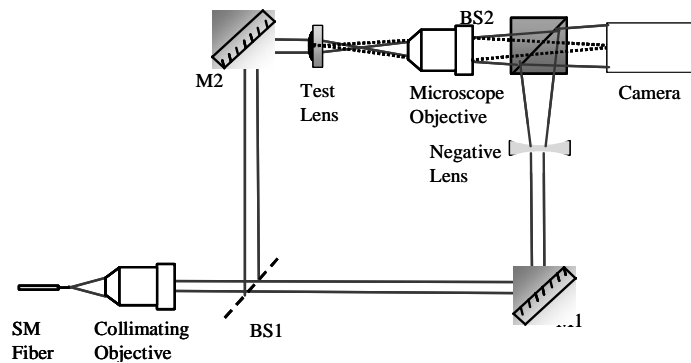


**Figure 2.13  Mach-Zehnder interferometer similar to the one used at NPL (from D. Daly and M.C. Hutley, "Micro-lens measurements at NPL").[39]**

For example, an interferometer used for evaluating micro-lenses at the National Physical Laboratory (NPL), the United Kingdom's national measurement laboratory, is shown schematically in figure 2.13. The aperture of the lens under test is imaged onto a camera by a microscope objective and relay lens. A well corrected lens pair in the reference path is used to match the curvature of the reference wavefront with that of the wavefront in the microscope objective. We have also chosen to use a Mach-Zehnder configuration to test the transmitted wavefront. The details of this system will be described in chapter three.

CHAPTER 3: INSTRUMENT DESIGN

The goal of the overall project was to design an interferometer that can be used to measure surface form, radius of curvature, transmitted wavefront, and back focal length of micro-refractive lenses.   The concentration of this thesis is on the transmitted wavefront calibration and measurement; however, the other applications had to be considered when choosing an appropriate design for the interferometer.

Of particular concern is the back focal length measurement.  It is determined by using a radius slide to measure the distance between the confocal position and the cat's eye position[13].  The *confocal position* is the position when the focal point of the lens under test coincides with the focal point of the reference objective.  It is located by measuring the transmitted wavefront (figure 3.1a).  The *cat's eye position* is position when the focal point of the reference objective is at the vertex of the lens (figure 3.1b).  It is measured in reflection and acts as a reference position for both the back focal length and radius of curvature measurements.
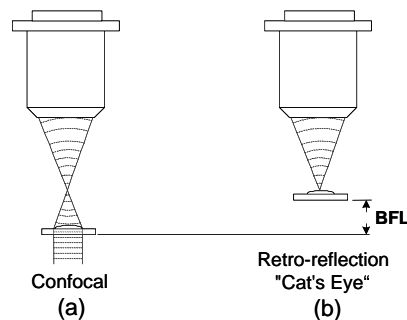


**Figure 3.1  Back focal length (BFL) measurement of a micro-lens using a radius slide.**

3.1.  Instrument Configuration

The configuration of the instrument must be easily changed for reflection or transmission measurements without disturbing the lens under test.  One solution is an instrument contains both a Twyman-Green and a Mach-Zehnder interferometer along with some convenient way to distinguish between the relevant interference pattern and those caused by other cavities (see figure 3.2).
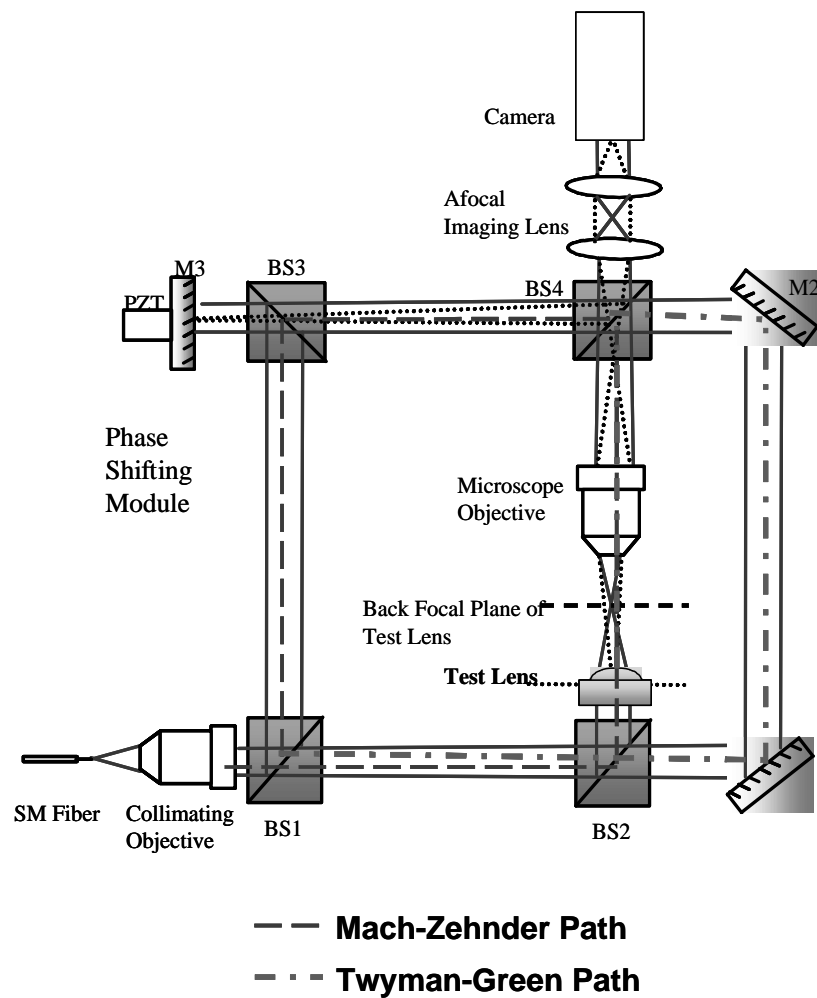


**Figure 3.2 Hybrid Mach-Zehnder/ Twyman-Green interferometer for measuring radius of curvature, form error, back focal length, and transmitted wavefront of a micro-lens.**

One solution is to use a source with low spatial coherence to localize the fringes. However, for micro-optics the back focal length is often small. The coherence length would need to be very short, making alignment difficult.[40] Therefore, the final design must incorporate some method to physically separate the Mach-Zehnder and Twyman-Green interferometers and allow the user to switch between the two configurations.

The design should minimize non-common path elements that could add bias by adding aberrations to the test or reference wavefront. If the elements are wavelength dependent then the systematic bias would also be wavelength dependent, requiring a separate calibration for each wavelength. The relative losses in the test and reference arm should also be considered so that good fringe contrast can be maintained.

The original concept for integrating the Mach-Zehnder and Twyman-Green interferometers (shown in figure 3.3) called for replacing BS1 in figure 3.2 with a fiber based splitter. In addition, the phase of the reference arm was to be shifted using a fiber based phase modulator such as a fiber wrapped tightly around a mandrel made of a piezoelectric material.[41] This would have greatly simplified the opto-mechanical requirements since the fiber could be routed around the microscope body in an arbitrary manner as long as an acceptable fiber bend radius is maintained.
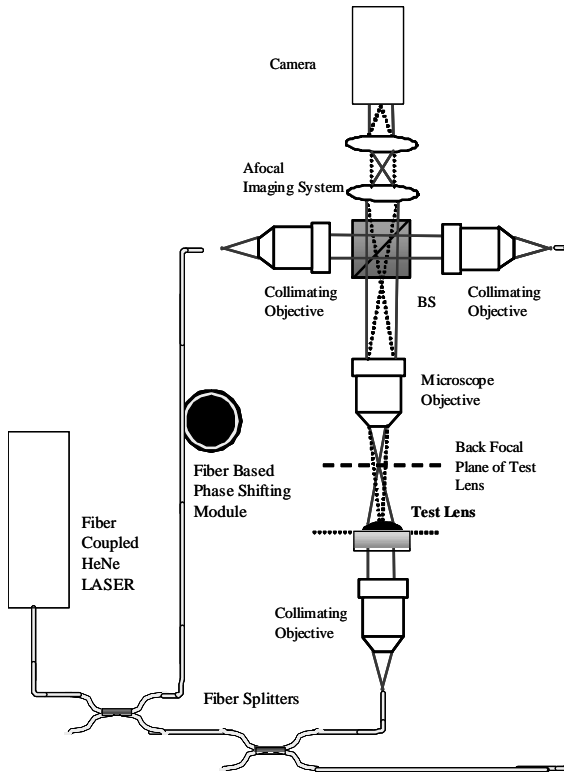
**Figure 3.3 Original concept for a hybrid Mach-Zehnder and Twyman-Green interferometer using fiber optics.**

However, the optical path length in the fiber is extremely sensitive to environmental conditions such as temperature and vibration. It was originally thought that a complicated phase compensation system would be necessary.[42] By protecting the fiber using furcation tubing, keeping the non-common path lengths as short a possible, and mechanically securing the fiber, using fiber without phase compensation proved suitable. Under normal operating conditions the fringe stability was comparable to other non-fiber based interferometers in the same laboratory, but phase shifting using a fiber based phase modulator complicated the system. We were not able to design a system to phase shift in fiber that would work for both interferometers.

Polarization optics can be used to separate the wavefronts reflected from different surfaces. For example, the quarter wave plate ($\lambda/4$) between the polarizing beam splitter

(PBS) and the microscope objective in figure 3.4 could be rotated to select either the reflected wavefront or the transmitted wavefront. The half wave plate ($\lambda/2$) could be rotated to adjust the relative intensities in the test and reference paths. If the quarter wave plate between the polarizing beam splitter and the microscope objective is rotated so that its slow axis is oriented at forty-five degrees with respect to the direction of linear polarization transmitted by the polarization beam splitter, then the light reflected from the surface of the device under test will be rotated ninety degrees when it reaches the polarization beam splitter on the return pass and would be reflected into the imaging system. The quarter wave plate in the reference arm allows the light reflected by the reference mirror to be transmitted to the imaging arm in a similar manner.
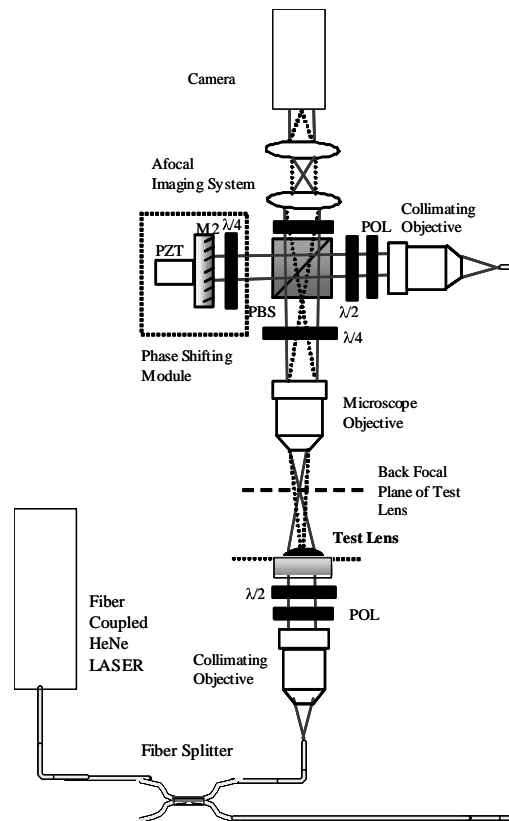


**Figure 3.4  Hybrid Twyman-Green and Mach-Zehnder interferometer based on polarization optics.**

If the quarter wave plate between the polarization beam splitter and the microscope objective is rotated so that the fast axis of the wave plate is aligned with the polarization axis of the polarization beam splitter, then the reflected light will not change polarization and will be transmitted back toward the source. However, light from the Mach-Zehnder test path will be split by the polarization beam splitter and some will be reflected into the imaging path.

The major drawback of this technique is that there are several components that are not common to both the test and reference paths. In addition, the retardance of the wave plates is extremely wavelength dependent.

The final system design can be viewed as inserting a fiber based Mach-Zehnder interferometer into a conventional Twyman-Green interferometer (see figure 3.5). In the Twyman-Green mode, a microscope objective is used to create a collimated beam from the fiber source. This beam is split into test and reference paths by BS2. The reference can be modulated using a mirror mounted on a piezoelectric transducer (PZT). This phase shift was performed using free space optics to avoid complications with keeping the system stable while phase shifting in the fiber. If a fiber-based phase shift is implemented in the future, the system would be similar to the original concept presented in figure 3.3. Since the source is both spatially and temporarily coherent, the location of this mirror is not critical. Beam splitter 3 (BS3) is not necessary for the Twyman-Green configuration and attenuates the reference beam and adds non-common path aberrations. However, this was an acceptable compromise considering the requirement that the system be able to operate in both a Twyman-Green and Mach-Zehnder configuration and that the system will be calibrated to remove instrument bias.

**Figure 3.5 Final system configuration used to measure form errors, radius of curvature, back focal length, and transmitted wavefront.**

For the transmitted wavefront measurement the source fiber is switched to the Mach-Zehnder path. This can be done without disturbing the alignment of any of the components in either the test or reference path. For the Mach-Zehnder configuration the test and reference paths are separated using a 50/50 biconic fiber splitter. The reference path is routed to a microscope objective which collimates the beam, and the beam is reflected by BS3 toward the reference mirror. The other output is routed to another microscope objective which creates a collimated beam that is directed to the entrance pupil of the lens under test. The position of the lens under test is adjusted along the optical axis so that the back focal plane of the test lens coincides with the focus of the microscope objective. The distance between lens 2 and lens 3 in the imaging lens system is adjusted so that the test lens aperture (or exit pupil) is imaged onto the camera.

## 3.2.   Imaging System Design

The purpose of the imaging system of any interferometer is to image the phase distribution of the test wavefront at a specific location onto the plane of the imaging sensor.  For surface form measurements the phase distribution of interest is the phase of the wavefront at the lens surface.  For transmitted wavefront measurements the phase distribution of interest is the normally the phase distribution at the exit pupil of the test lens.   This presents a problem when attempting to measure the form of a lens with a radius of curvature much smaller than the focal length of the reference objective or the transmitted wavefront of a lens (or lens system) with back focal lengths much smaller than that of the objective (see figures 3.6 and 3.8) because the distance from the reference objective to the image becomes large (see figure 3.7).
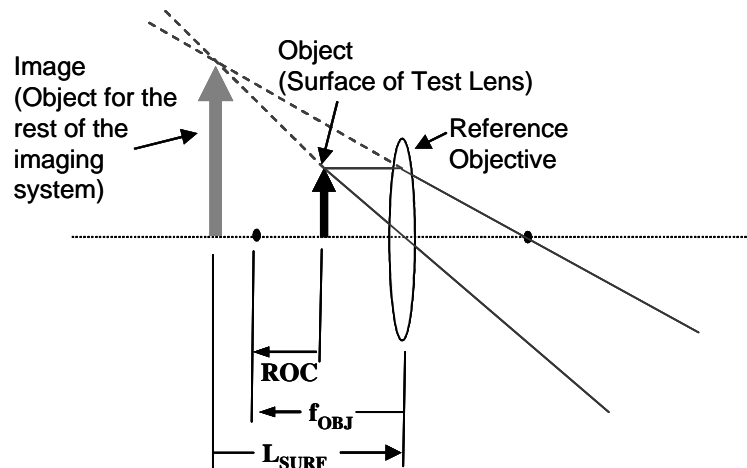


**Figure 3.6   For form measurements, the lens under test is placed so that its center of curvature coincides with the focal point of the reference objective.    The image of the test lens surface must be relayed to the imaging sensor.**
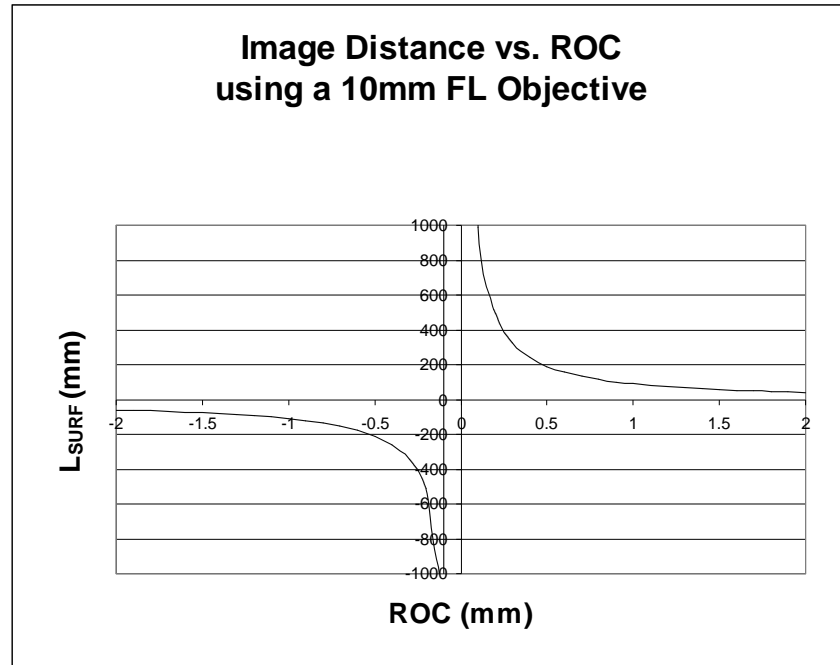
**Figure 3.7  If  the radius of curvature is small compared with the focal length of the objective then L$_{SURF}$ becomes large.**

In designing the imaging system for this interferometer, we followed the method described by Schwider[43] to design the imaging system of a Twyman-Green interferometer used to measure the radius of curvature of micro-lenses.  The problem is broken up into two sections.  First, the location of the image of the test lens surface or exit pupil formed by the reference objective is determined.  The location of the lens aperture with respect to the microscope objective is fixed by the radius of the lens (or the back focal length of the lens) and the focal length of the objective (see figure 3.6 and 3.8).  The rest of the imaging system is designed using this intermediate image as the object.  This also determines the proper location of the reference mirror for optimum contrast with partially coherent sources.
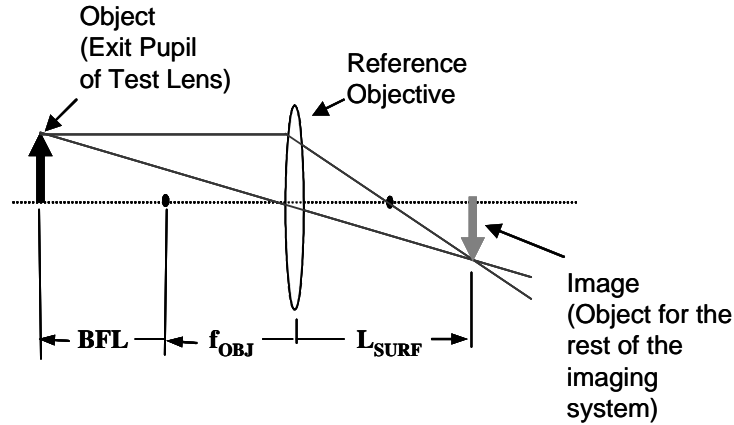
**Figure 3.8 For transmitted wavefront measurements, the lens under test is placed so that its back focal point coincides with the focal point of the reference objective. The image of the lens aperture formed by the objective must be relayed to the imaging sensor. However, just like for a small ROC, if the back focal length of the test lens is small compared to the focal length of the objective then $L_{SURF}$ becomes very large.**

The location of the paraxial image of the aperture is given by:

$$\frac{1}{L_{SURF}} = \frac{1}{f_{OBJ}} - \frac{1}{f_{OBJ} + BFL}$$

**(3.1)**

so that the magnification due to the objective is:

$$M_{OBJ} = \frac{L_{SURF}}{f_{OBJ} + BFL}$$

**(3.2)**

If the objective is fixed at a distance $L_{FIXED}$ from the first lens in the imaging system, then the location of the intermediate image, $L_{OBJ}$, in figure 3.9 is given by:

$$L_{OBJ} = L_{FIXED} - L_{SURF}.$$

**(3.3)**
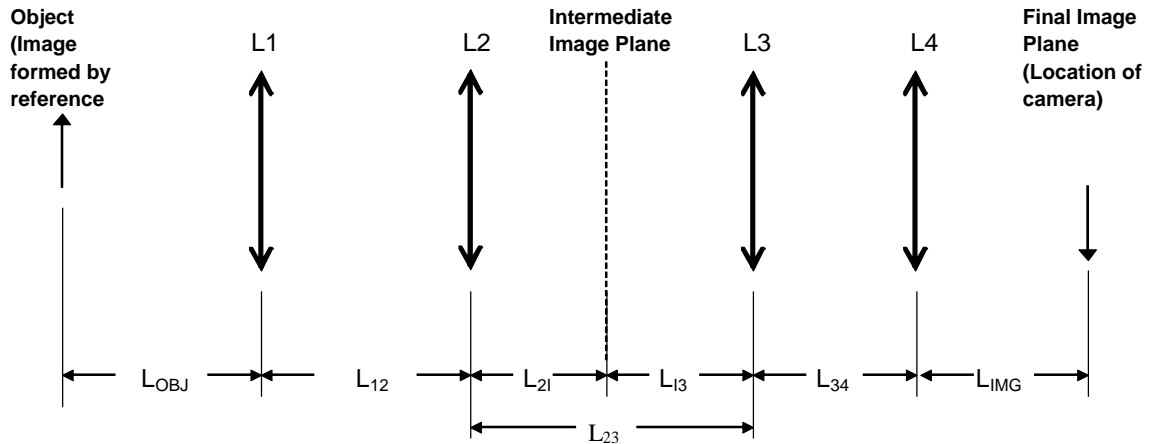
**Figure 3.9 Definition of the variables used to design the imaging system.**

We chose to use two afocal telescopes to image this object (the image formed by the reference objective) onto the camera (see figure 3.9). The first telescope (consisting of lens L1 and lens L2) forms an image at an intermediate plane. This image may be virtual (see figure 3.10). The second telescope (consisting of lens L3 and lens L4) relays this image onto the camera. This must be a real image. The distance from L1 to the reference objective and the distance from L4 to the camera are fixed. The distance between L2 and L3 can be adjusted to focus the system.

Afocal systems can be formed using two lenses with a common focal point.[44] These systems have zero power and an undefined focal length. The transverse magnification of the pair of lenses is equal to the ratio of their focal lengths (see equation 3.4). Therefore the magnification of the imaging leg can be changed simply by replacing a lens in one of the telescopes independent of position of the intermediate image. The magnification is also insensitive to the axial position of the afocal system. The system can be made telecentric by placing the stop at the common focal point.[45]
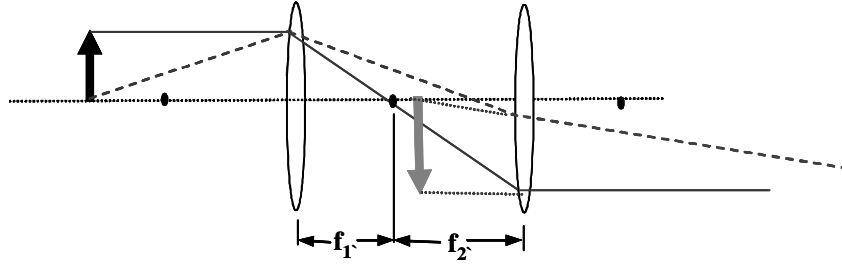
**Figure 3.10 An afocal system used at finite conjugates. Notice that for an object outside the focal length of the first lens the final object is virtual.**

Since Lens 1 and Lens 2 form an afocal system, the magnification of the lens pair

is simply the ratio of their focal lengths

$$M_{12} = \frac{f_2}{f_1}$$

(3.4)

and the distance between Lens 1 and Lens 2 is the sum of their focal lengths

$$L_{12} = f_1 + f_2.$$

(3.5)

Similarly, for Lens 3 and Lens 4

$$M_{34} = \frac{f_4}{f_3}$$

(3.6)

and

$$L_{34} = f_3 + f_4.$$

(3.7)

This gives the combined magnification of the afocal imaging systems as:

$$M_{SYS} = M_{34}M_{12}$$

(3.8)

so that the total magnification is:

$$M_{TOT} = M_{SYS} M_{OBJ}$$

(3.9)

With the total magnification, the percentage the CCD filled by the image of the lens is:

$$CCDFill = M_{TOT} \frac{\phi}{CCDSize}$$

(3.10)

where *CCDSize* is the size of the CCD active area along the smallest (typically horizontal) dimension and $\phi$ is the clear aperture of the lens under test.

CHAPTER 4:  SELF-CALIBRATION USING A BALL LENS: METHODOLOGY

By averaging the transmitted wavefronts from a randomly positioned ball lens we have developed a self-calibration technique for transmitted wavefront measurements in a Mach-Zehnder configuration.  The contributions due to form errors and random index of refraction variations of the ball will average to zero, however, a ball lens adds spherical aberration to the wavefront.  For an infinite conjugate system, the expected contribution to the spherical aberration, with an associated uncertainty, can be calculated from the ball diameter and index of refraction, and the aperture size of the system.  This calculated value can be subtracted from the averaged data to determine the systematic bias of the interferometer.

The transmitted wavefront may be represented by the phase of the wavefront at each point in the field, the coefficients of an orthonormal set of polynomials, a statistical description, or some other mathematical means.  We have chosen to use Zernike polynomials, due not only to their widespread acceptance in optical testing, but also because it is relatively simple to separate rotationally invariant terms from the data set. The phase of the wavefront at a point in the aperture is represented by[46,47,48]

$$W(\rho,\theta) = \sum_{r=1}^{L} A_r U_r$$

**(4.1)**

where $\rho$ and $\theta$ are the normalized polar coordinates of the point, $L$ is the number of

Zernike terms used to approximate the surface, $A_r$ is the $r^{th}$ Zernike coefficient and

$U_r(\rho,\theta)$ is the $r^{th}$ Zernike polynomial as defined in table 4.1 for the first thirty-six terms.

**Table 4.1   Fist 36 University of Arizona Zernike polynomials with term numbers as used in this thesis.**[46,47]

| Term Number (r) | Zernike Polynomial ($U_r$) | Physical Meaning |
|---|---|---|
| 1 | $1$ | Piston |
| 2 | $\rho \cos(\theta)$ | Tilt in X Direction (0 degrees) |
| 3 | $\rho \sin(\theta)$ | Tilt in Y Direction (90 degrees) |
| 4 | $2\rho^2 - 1$ | Power |
| 5 | $\rho^2 \cos(2\theta)$ | Astigmatism at 0 or 90 degrees |
| 6 | $\rho^2 \sin(2\theta)$ | Astigmatism at +/- 45 degrees |
| 7 | $(3\rho^2 - 2)\rho \cos(\theta)$ | Coma Along Y Axis |
| 8 | $(3\rho^2 - 2)\rho \sin(\theta)$ | Coma Along X-Axis |
| 9 | $6\rho^4 - 6\rho^2 + 1$ | Third Order Spherical |
| 10 | $\rho^3 \cos(3\theta)$ | |
| 11 | $\rho^3 \sin(3\theta)$ | |
| 12 | $(4\rho^2 - 3)\rho^2 \cos(2\theta)$ | |
| 13 | $(4\rho^2 - 3)\rho^2 \sin(2\theta)$ | |
| 14 | $(10\rho^4 - 12\rho^2 + 3)\rho \cos(\theta)$ | |
| 15 | $(10\rho^4 - 12\rho^2 + 3)\rho \sin(\theta)$ | |
| 16 | $20\rho^6 - 30\rho^4 + 12\rho^2 - 1$ | Fifth Order Spherical |
| 17 | $\rho^4 \cos(4\theta)$ | |
| 18 | $\rho^4 \sin(4\theta)$ | |
| 19 | $(5\rho^2 - 4)\rho^3 \cos(3\theta)$ | |
| 20 | $(5\rho^2 - 4)\rho^3 \sin(3\theta)$ | |
| 21 | $(15\rho^4 - 20\rho^2 + 6)\rho^2 \cos(2\theta)$ | |
| 22 | $(15\rho^4 - 20\rho^2 + 6)\rho^2 \sin(2\theta)$ | |
| 23 | $(35\rho^6 - 60\rho^4 + 30\rho^2 - 4)\rho \cos(\theta)$ | |
| 24 | $(35\rho^6 - 60\rho^4 + 30\rho^2 - 4)\rho \sin(\theta)$ | |
| 25 | $70\rho^{8} - 140\rho^{6} + 90\rho^4 - 20\rho^2 + 1$ | Seventh Order Spherical |
| 26 | $\rho^5 \cos(5\theta)$ | |
| 27 | $\rho^5 \sin(5\theta)$ | |
| 28 | $(6\rho^2 - 5)\rho^4 \cos(4\theta)$ | |
| 29 | $(6\rho^2 - 5)\rho^4 \sin(4\theta)$ | |
| 30 | $(21\rho^4 - 30\rho^2 + 10)\rho^3 \cos(3\theta)$ | |
| 31 | $(21\rho^4 - 30\rho^2 + 10)\rho^3 \sin(3\theta)$ | |
| 32 | $(56\rho^6 - 105\rho^4 + 60\rho^2 + 10)\rho^2 \cos(2\theta)$ | |
| 33 | $(56\rho^6 - 105\rho^4 + 60\rho^2 + 10)\rho^2 \sin(2\theta)$ | |
| 34 | $(126\rho^8 - 280\rho^6 + 210\rho^4 - 60\rho^2 + 5)\rho \cos(\theta)$ | |
| 35 | $(126\rho^8 - 280\rho^6 + 210\rho^4 - 60\rho^2 + 5)\rho \sin(\theta)$ | |
| 36 | $252\rho^{10} - 630\rho^8 + 560\rho^6 - 210\rho^4 + 30\rho^2 - 1$ | Ninth Order Spherical |

4.1.   Determining the System Bias

For each measurement in the calibration, the measured wavefront ($W_i$) will be a combination of the systematic bias of the interferometer, the wavefront aberrations due to the ball lens, and noise.

$$W_i = W_{INT} + W_{i,BALLFigure}(\rho,\theta) + W_{BALLSpherical}(\rho) + W_{i,NOISE}$$

**(4.2)**

where $W_{INT}$ is the systematic bias in the measurement due to the interferometer, $W_{iBALLFigure}(\rho,\theta)$ is the contribution to the ith measurement due to the figure error (and homogeneity variations) of the ball lens, $W_{BALL}(\rho)$ is the contribution due to the inherent spherical aberration of the ball lens, and $W_{NOISE}$ is the random noise in the system.  If the ball lens is truly spherical, homogeneous, and centered on the optical axis, there will be no rotational dependence of the transmitted wavefront.  For a real ball lens there will be variations to this symmetry due to form errors, surface roughness, and index inhomogeneities.  However, if the ball lens in positioned in random orientations and a sufficient number of wavefronts are averaged, the effect will be to eliminate the randomly varying components.[51]  The contributions due to the random noise is also zero on average.  Thus,

$$\frac{1}{N}\left(\sum_{i=1}^{N} W_{i,BALLFigure}(\rho,\theta) + \sum_{i=1}^{N} W_{i,NOISE}\right) \to 0$$

**(4.3)**

as $N$, the number of the measurements that are averaged, approaches infinity.  We can then solve for the systematic bias

$$W_{INT} = \frac{1}{N}\sum_{i=1}^{N}(W_i) - W_{BALLSpherical}(\rho)$$

.

### 4.2. Estimating the Uncertainty

For the randomly varying components, the random contributions of the ball lens and the noise, a reasonable estimate of the standard uncertainty is the standard deviation of each Zernike coefficient obtained from fitting the measured data.  As shown in section 2.1, the sensitivity coefficient for this source of uncertainty is the inverse square root of the number of measurements.  The components due to the inherent spherical aberration of the ball lens, $W_{BALLSpherical}(\rho)$, can be calculated from the diameter of the aperture, the index of refraction of the ball lens, and its radius of curvature, each with an associated uncertainty.  We used ZEMAX® optical design software to perform the calculation.  An estimate of the uncertainty in the calculated Zernike terms was obtained by randomly varying the input parameters over a reasonable range as determined from manufacture specifications.  These uncertainty estimates are discussed in more detail with an example in section 5.3.

As formulated in this thesis, the self calibration technique treats each individual Zernike coefficient as a measurand.  The result is a set of biases in Zernike coefficients along with stated uncertainties.  In general, the expectation of a linear function can be related to the expectations of each term by[52]

$$E[ax + by + cz + ...] = aE[x] + bE[y] + cE[z] + ...$$

.

Applying equation 4.5 to the first few terms of equation 4.1, the Zernike expansion of the

wavefront, the expectation of the bias for any particular point in the pupil is

$$E[W_{INT}(\rho, \theta)] = E[A_1] + E[A_2]\rho\cos(\theta) + E[A_3]\rho\sin(\theta) + \ldots$$

**(4.6)**

where $A_i$ is the coefficient of the $i^{th}$ term in the Zernike polynomial. The surface

calculated from the average of the Zernike coefficients found by fitting $N$ phase maps is

equivalent to the Zernike coefficients found by fitting the point by point average of those

$N$ phase maps. However, contributions to the bias from spatial frequencies described by

higher order Zernike coefficients than those carried through the procedure are lost.

Appling equation 2.13, the combined standard uncertainty for the calculated bias at any

particular point in the pupil is

$$u_c(W_{INT}) = \sqrt{u^2(A_1) + u^2(A_2)[\rho\cos(\theta)]^2 + u^2(A_3)[\rho\sin(\theta)]^2 \ldots}.$$

**(4.7)**

Notice that the combined uncertainty in the phase is dependent on the aperture position.

CHAPTER 5: SELF-CALIBRATION USING A BALL LENS: IMPLEMENTATION

To demonstrate the technique, the interferometer shown in figure 5.1 was calibrated for measuring a micro-refractive lens with a 0.14 NA. The calibration wavefront will not be correct if the numerical aperture (NA) of the ball lens/pinhole assembly used for the calibration is not equal to the numerical aperture of the lens that will be tested. Since we are using a set of Zernike coefficients to represent the system bias, if the numerical aperture of the test lens does not match the  do not match the numerical aperture of the ball lens/aperture used to calibrated the system, then the wavefront that is calculated from the calibration and subtracted from the measurement will be radially sheared with respect to the actual system bias. If we assume that the dominant biases in the interferometer come from the objective lens, the percent error due to this NA mismatch ($\sigma_{rad}$) is equal to the relative sensitivity of a radial shearing interferometer. This can be approximated by[49]

$$\sigma_{rad} = 1 - R^4$$

**(5.1)**

where R is the radial shear. In this case $R$ is equal to the ratio of the NAs. This is a worst-case approximation so that, for an error in the calibration factor of less than 1%, the NA of the ball lens/pinhole aperture used for the calibration should be within 4% of the NA of any of the lenses that will be tested.

A Mitutoyo M Plan Apo 10 objective with an NA of 0.28 was chosen from the available selection to maximize the size of the image of the aperture on the camera. The measurements were performed at a wavelength of 632.8 nm.  An 800 micrometer aperture and 4 millimeter BK7 ball lens, resulting in an NA of 0.135, satisfies the 4% guideline and was chosen for availability and ease of handling.  The phase-shifted interferograms are analyzed using IntelliWave™ from Engineering Synthesis Design and fit to a set of Zernike polynomials.
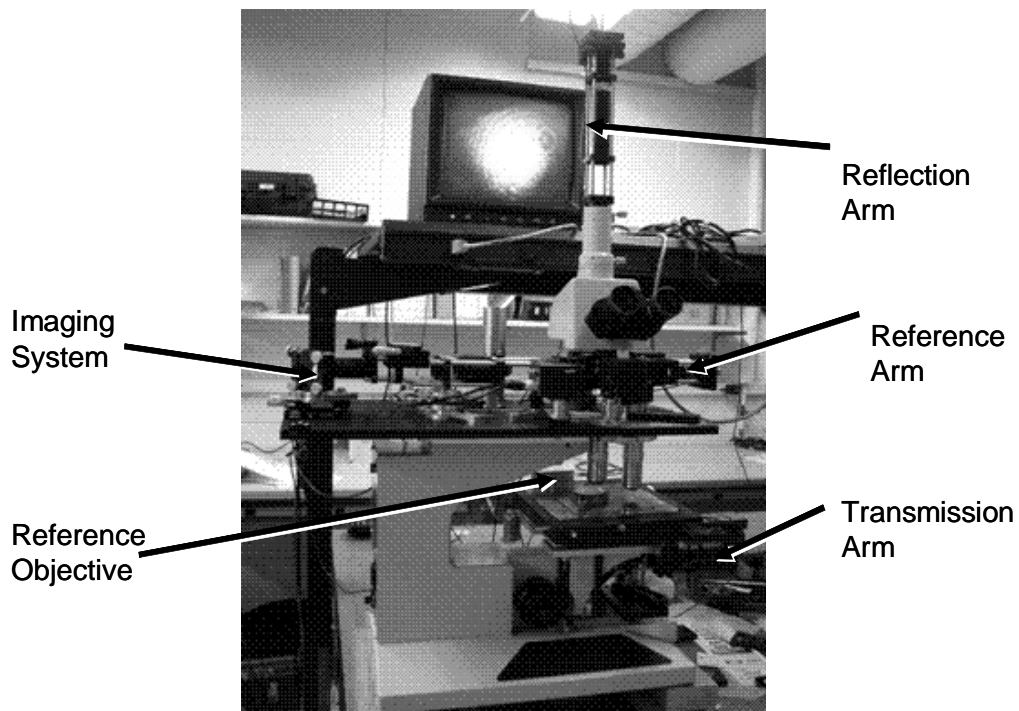


**Figure 5.1  Picture of the interferometer used to demonstrate of the technique.**

## 5.1.   Experimental Design

Three calibration runs were conducted according to the procedure outlined in Appendix A.  The ball lens was held in a depression at the center of a pin hole aperture. Between each sample the ball lens was perturbed by blowing on it with a puff of air from a lens blower brush and allowed to randomly settle back into the depression around the

aperture.  Each run contained sixty five samples of the transmitted wavefront measured with the ball lens at random orientations.  The number of samples was based on a balance between the incremental reduction in the uncertainty of the bias estimate from ball lens figure errors (as discussed in section 5.3.1) and practical considerations such as the time required to complete the experiment.  Between each calibration run the ball lens and aperture were removed and realigned in the interferometer.  During each run some of the samples were measured thirty times without changing the lens position in order to gauge the repeatability of the measurements (only one of these measurements was included in the sample set used for the calibration run).  Figure 5.2 shows an example of an interferogram and phase map from a single measurement.
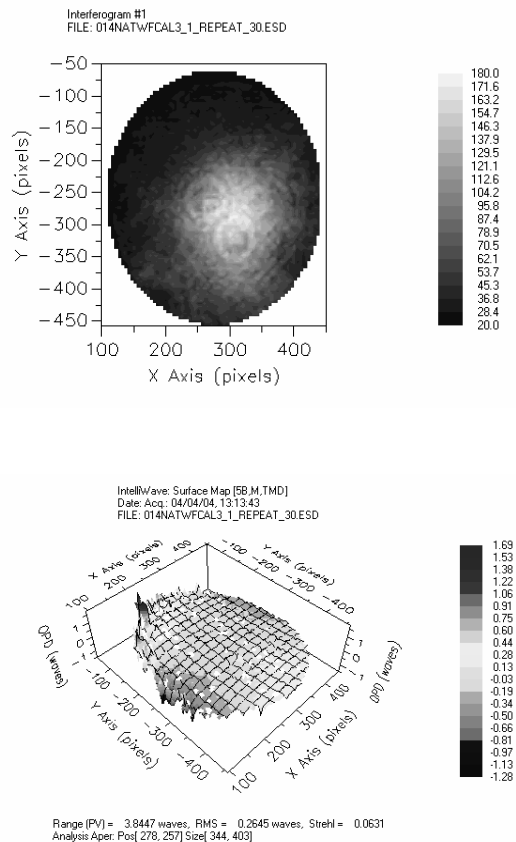


**Figure 5.2  Example of an interferogram and computed phase map from a single measurement.**

Prior to the third calibration run the ball lens/aperture was systematically decentered and defocused to experimentally determine the measurement's sensitivity to misalignment of the ball lens/aperture assembly. After the last calibration run, the ball lens/aperture assembly was left in place and measurements were taken approximately every ten minutes over a ninety minute period to determine the stability of the measurements during a single calibration run. The experimental design used to determine the results presented in this thesis is summarized in table 5.1.

**Table 5.1  Experimental design used to determine the bias of the Zernike Coefficients**

| Run | Sample | Description | Number of Samples | Number of Meas. |
|---|---|---|---|---|
| 1 | 52 | Repeatability test for 52nd sample in first calibration run | | 30 |
| 1 | | First calibration run | 65 | |
| 2 | 1 | Repeatability test before beginning second calibration run | | 30 |
| 2 | | Second calibration run | 65 | |
| - | | Laterally misaligned ball lens/aperture and recorded measurements with various tilt in both directions | | 31 |
| - | | Axially misaligned ball lens/aperture and recorded measurements at various focus positions | | 21 |
| - | | Repeatability test before beginning first attempt at the fourth calibration run | | |
| 3 | 1 | Repeatability test before beginning the third calibration run | | 30 |
| 3 | 35 | Repeatability test for the 35th sample in the third calibration run | | 30 |
| 3 | 70 | Repeatability test for the 70th sample in the third calibration run | | 30 |
| 3 | | Third calibration run | 65 | |
| 3 | 70 | Measurments taken every 10 minutes over a 90 minute period without moving the ball lens. | | 10 |

Notes:  Removed and realigned ball lens/aperture between each calibration run
Randomly repositioned ball lens between each sample
Averaged 10 phase maps and fit 36 Zernike polynomials for each measurement

Repeatability tests were conducted by measuring the ball lens/aperture 30 times without repositioning the ball lens (Note:  only one measurement from each repeatability test was included in the calibration.)

Table 5.1 does not represent all of the measurements taken during the experiment. Some samples from the first and third calibration runs were truncated to simplify the data

analysis, an initial calibration run was not included because the data mask was moved, and an initial attempt at the third calibration run was aborted because the microscope translation stage moved.

## 5.2. Repeatability, Reproducibility, and Stability

The repeatability and reproducibility of the measurements were determined from the five sets of thirty measurements that were made without moving the ball lens. The data were analyzed using and an analysis of variance (ANOVA) technique[53] to separate the repeatability of a measurement within one sample, the reproducibility of the measurements between samples, and the reproducibility of the bias estimate between calibration runs.

The repeatability of the measurement within one sample is the average standard deviation of the thirty measurements. This average standard deviation is equivalent to the standard deviation of the noise term in equation 4.2. It is the instrument's contribution to the standard uncertainty of the measurements $u(W_i)$ in table 5.2.

The reproducibility of the measurements between samples was determined by taking the standard deviation of the average of the thirty measurements for different samples within the same calibration run. By averaging the thirty measurements for each sample, the effects of random noise within one measurement is decreased leaving the effect of randomly orienting the ball along with drifts in the instrument contributions and noise between samples. This is also part of $u(W_i)$.

The reproducibility of the measurements between calibration runs was determined by taking the standard deviation of the averages of the thirty measurements of a single sample from each calibration run.

Finally, the stability of a single measurement over the time period needed to conduct the calibration run was determined by taking the standard deviation of measurements from a single sample over a ninety minute period. The random portion of this variation is equivalent to the noise in a single measurement and is included in $u(W_i)$. Long term drift of the instrument on a timescale larger than the time period of the calibration was not investigated in this study. If the long term drift of the instrument leads to fluctuations larger than that observed in the stability investigation carried out here, then an additional bias in the calibration will be present. This should be investigated in the future. An example of the drift data is shown in figure 5.3. There is no indication of a gradual long term drift, therefore it is likely that the fluctuation observed during the calibration run are included in $u(W_i)$.
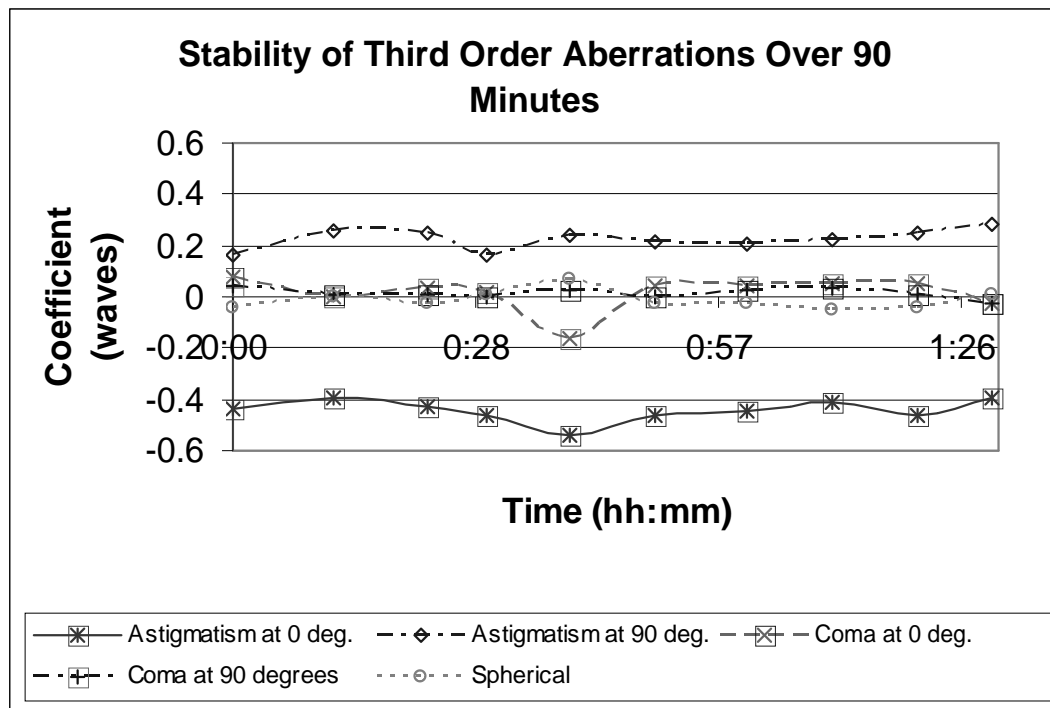


**Figure 5.3 Plot of stability of third order aberrations over the period required for one calibration run, showing the stability of the instrument can be included with $u(W_i)$.**

5.3.    Uncertainty Estimate

The contributions of the uncertainty sources to the combined uncertainty of the bias estimate  are assumed to be statistically independent and linear so that the combined uncertainty of the bias estimate is simply the square root of the sum of the squares of the individual standard uncertainties times the associated sensitivity coefficients.[54]    The sources of uncertainty and their relative contributions to the combined uncertainty for one Zernike coefficient are summarized in table 5.2.  Similar tables were created for all of the first thirty-six Zernike coefficients.  The results are summarized in chapter 6.  The remainder of this chapter provides an explanation of each source of uncertainty and the assumptions and methods used to determine the standard uncertainty, distribution factor, and sensitivity coefficients.

**Table 5.2 The uncertainty analysis for Zernike term 5 (0 degree astigmatism)**

Term 5            Bias Estimate:      -0.413 waves

| Uncertainty Source $x_i$ | Reference | Type | Stated Uncertainty | Distribution Factor | Standard Uncertainty | Sensitivity Factor $(\delta f/\delta x_i)$ | Contribution to Combined Uncertainty $u(x_i)$ | Degrees of Freedom $\nu(x_i)$ |
|---|---|---|---|---|---|---|---|---|
| Ball Lens Figure Errors and Noise $(W_i)$ | §5.3.1 | A | 0.064 λ | 1 | 0.064 λ | 0.12403473 | 0.008 | 20 |
| Inherent Spherical Aberration $(W_{BALLSpherical})$ | §5.3.2 | B | λ | 1 | λ | 1 | | |
| Aperture Misalignment | §5.3.3 | A | | | | | | |
| Lateral Misalignment | | | 0.071 λ | 1 | 0.071 λ | 0.06 | 0.004 | |
| Axial Misalignment | | | 0.020 λ | 1 | 0.020 λ | 0.49 | 0.010 | |
| Aperture Tilt | §5.3.4 | B | 0.003 λ | 1 | 0.003 λ | 1.00 | 0.003 | |
| Ball Lens Misalignment | §5.3.5 | B | 0.101 λ | 1 | 0.101 λ | 0.7555 | 0.077 | |
| NA Mismatch | §5.3.6 | B | 0.413 λ | 1 | 0.413 λ | 0.01 | 0.004 | |
| | | | | | | | | |
| | | | | | | | | |
| | | | | | | | | |
| | | | | Combined Variance; $u_c^2(y)$: | | | 0.006 waves$^2$ | |
| | | | | Combined Uncertainty; $u_c(y)$: | | | 0.078 waves | |
| | | | | Effective Degrees of Freedom; $\nu_{eff}(y)$: | | | 186379 | |
| | | | | Coverage Factor: | | | 2.000 | |
| | | | | Expanded Uncertainty; $U_p$: | | | **0.156 waves** | |
| | | | | Level of Confidence; $P$: | | | **95.45 %** | |

### 5.3.1. Ball Lens Figure Errors and Noise ($W_i$)

For the randomly varying components, a reasonable estimate of the standard uncertainty is standard deviation of each Zernike coefficient obtained from fitting the measured data. The samples from the second calibration run were used to calculate this standard deviation. As shown in section 2.1, the sensitivity coefficient for this source of uncertainty is the inverse square root of the number of measurements. Therefore, its contribution to the combined uncertainty decreases if more samples are used to calculate the average. However, there are practical considerations such as the time required to complete the calibration. In addition, the incremental reduction in the sensitivity coefficient diminishes as the number of samples is increased. For example, if thirty samples are used to calculate the average, the sensitivity coefficient is 0.182. If thirty-one samples are used, the sensitivity coefficient is 0.173. The incremental difference in the sensitivity coefficient between using thirty samples and using thirty-one samples is 0.003. The incremental difference between using sixty-four samples and using sixty-five samples is 0.001. We chose to use sixty-five samples so that the contribution to the combined uncertainty in the bias estimate due to the ball lens figure errors and noise is comparable to the contributions form the other sources of uncertainty. The value of one of the coefficients over seventy measurements is shown in figure 5.4a. The running average, shown in figure 5.4b, indicates that the average value of the coefficient converges as the contributions due to the figure errors of the ball lens approach zero.
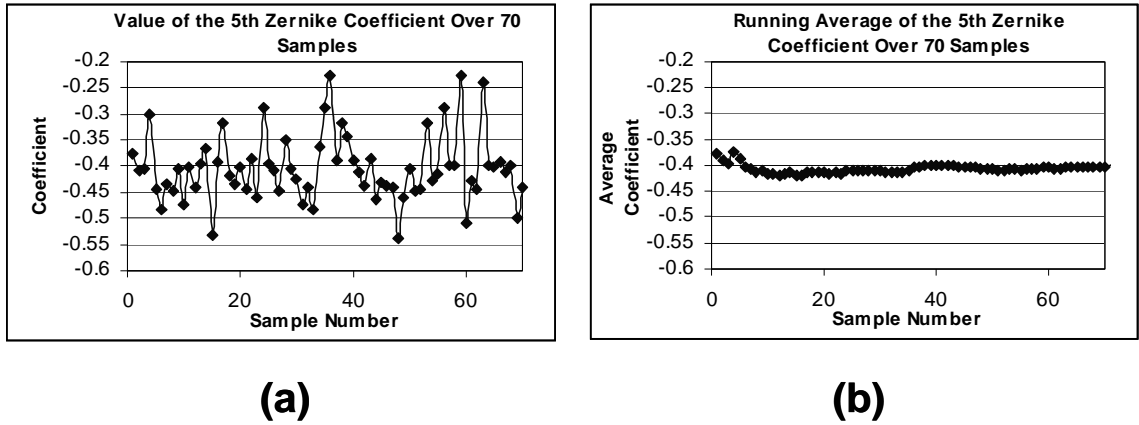
Figure 5.4 Graph of on polynomial coefficient over 70 samples (a) and running average of these values (b) indicate that the values are random and that the average converges.

### 5.3.2. Inherent Spherical Aberration *(W_BallSpherical)*

The components due to the inherent spherical aberration of the ball lens, $W_{BALLSpherical}(\rho)$, can be calculated from the diameter of the aperture, the index of refraction of the ball lens, and its radius of curvature, each with an associated uncertainty. We used ZEMAX® optical design software to perform the calculation. The stop size was defined by setting the entrance pupil diameter. A paraxial lens is used to image the aperture stop onto the image plane and the position of the image plane is determined by solving for a marginal ray height of zero. The model is summarized in figure 5.5.

| Type | Comment | Radius | Thickness | Glass | Diameter |
|------|---------|--------|-----------|-------|----------|
| OBJ | STANDARD | Infinity | Infinity | | 0 |
| 1 | STANDARD | Infinity | 5 | | 0.8 |
| STO | STANDARD | Infinity | 0 | | 0.8 |
| 3 | STANDARD | 2 | 2 | BK7 | 4 |
| 4 | STANDARD | Infinity | 2 | BK7 | 0.52928 |
| 5 | STANDARD | -2 | 2 | | 4 |
| 6 | PARAXIAL | - | 18.06814 | | 0.302838 |
| IMA | STANDARD | Infinity | | | 0.152672 |



Figure 5.5 ZEMAX® model for the ball lens and aperture with a NA =0.14.

An estimate of the uncertainty in the calculated Zernike terms was obtained by randomly varying the input parameters over a reasonable range as determined from manufacture specifications using a Monte Carlo simulation.  The ball diameter, index of refraction, an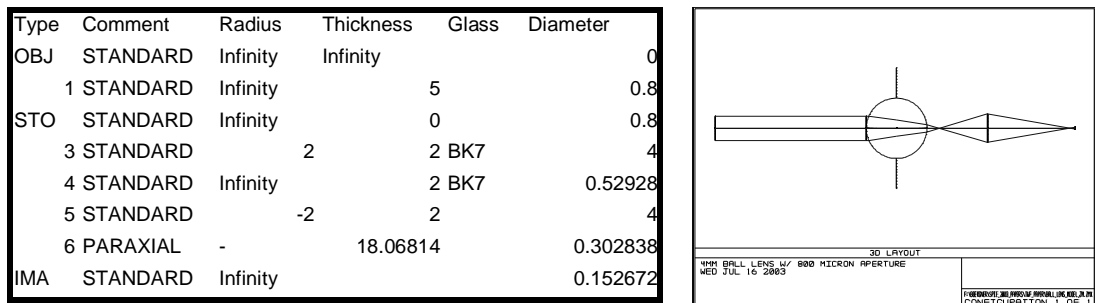d the aperture size of the system were varied over a normal distribution with a standard deviation of 1% for the index of refraction, 2.5 microns for the ball diameter, and 5 microns for the aperture diameter (see figure 5.6).

| Tolerarance Data Editor | | | | | | | |
|---|---|---|---|---|---|---|---|
| # Type | Int1 | Int2 | Int3 | Nominal | Min | Max | Comment |
| 1 STAT | | 0 | 2 - | - | - | - | |
| 2 TIND | | 5 - | - | 1.5168 | -0.01768 | 0.017682 | 1% index |
| 3 TRAD | | 5 - | - | 2 | -0.00127 | 0.00127 | 2.5 um ball diameter |
| 4 TMCO | | 1 | 1 - | 0.8 | -0.005 | 0.005 | 5um EPD |

**Figure 5.6  Tolerance data as used by ZEMAX® to estimate the uncertainty in the inherent spherical aberration of the ball lens.**

### 5.3.3.   Aperture Misalignment

The ball lens is held in place with a pinhole aperture that also acts as the aperture stop for the system.  We defined the optical axis of the interferometer to be perpendicular to the incident wavefront and nominally centered on this aperture (see Figure 5.7).  The lateral position of the optical axis is fixed by the software mask that defines the unit circle over which the software fits the Zernike coefficients.   Any misalignment of the microscope objective or other optics with respect to this axis contributes to the  bias.  If the aperture or  ball lens is not aligned with the optical axis of the interferometer,  the ball lens will no longer introduce only spherical aberration to the wavefront.   This misalignment  will contribute to an uncertainty in the bias estimate.
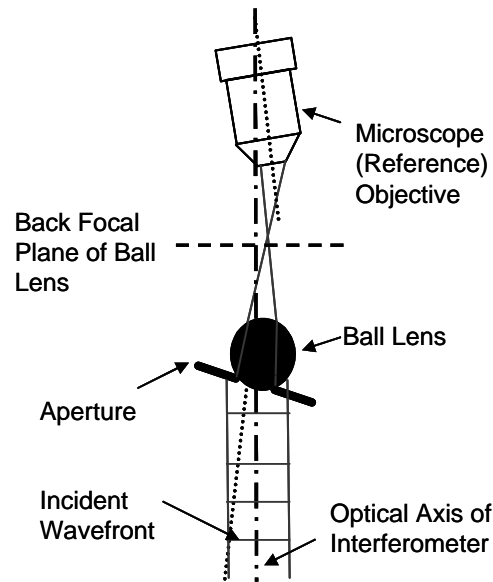
**Figure 5.7    Misalignment of the ball lens and aperture with respect to the optical axis of the interferometer introduces an uncertainty into the estimate of the bias.**

Lateral misalignment of the ball and aperture with respect to the optical axis of the interferometer will manifest itself as tilt in the wavefront. It will also contribute to higher order aberrations since the ball lens/aperture system is no longer symmetric about the axis of the measurement. To determine the sensitivity of the bias estimate to lateral misalignment of the aperture, the ball lens/aperture was systematically misaligned by moving the microscope translation stage. Since it was not practical to add tilt to the wavefront along only one axis, the square root of the sum of the squares of the individual tilt coefficients was used as a measure of combined tilt. The values of the Zernike coefficients were plotted against the combined tilt (see figure 5.8). Assuming that the relationship between the each Zernike coefficient and the combined tilt is linear over the region of interest, the ratio of the standard deviation of the coefficient to the root mean square of the standard deviations of the tilt coefficients can be used as a measure of the sensitivity of the coefficient to lateral misalignment of the aperture as measured by the

combined tilt.  The standard uncertainty for the lateral misalignment is set by the initial

alignment of the system as described in step 8 of the calibration procedure (see Appendix

A).  Axial misalignment can be treated in a similar manner using the Zernike power term.
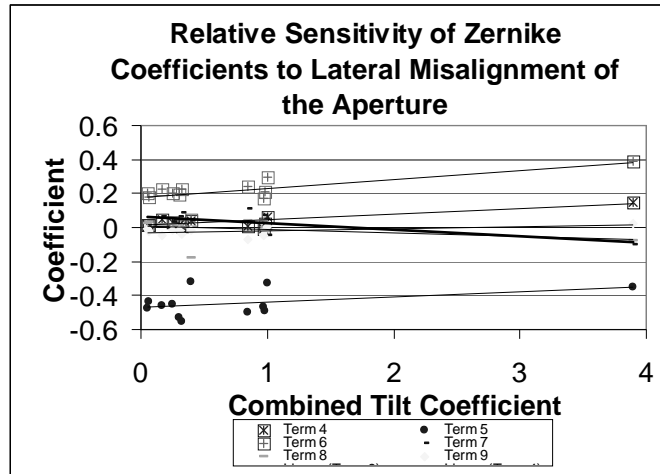


**Figure 5.8  Plot of Zernike coefficients with respect to the combined tilt coefficient (the square root of the sum of the squares of the tilt coefficients) including linear trend lines.**

### 5.3.4.   Aperture Tilt

The contribution to the uncertainty in the bias estimate due to tilt of the aperture

with respect to the axis of the interferometer was estimated using the ZEMAX® tolerance

feature.  We assumed that we could visually align the aperture perpendicular to the axix

of the interferometer within two degrees.  The  standard uncertainty is the standard

deviation of the coefficient obtained from a Monte Carlo simulation in which the tilt of

the aperture/ball lens system about the x and y-axis were varied simultaneously over a

uniform distribution with a standard deviation of two degrees (see figure 5.9).

| # | Type | Int1 | Int2 | Int3 | Nominal | Min | Max | Comment |
|---|------|------|------|------|---------|-----|-----|---------|
| | 1 TETX | | 2 | 5 - | - | | -2 | 2 X Tilt of Aperture/Ball Lens (+/- 2 degrees) |
| | 2 TETY | | 2 | 5 - | - | | -2 | 2 Y Tilt of Aperture/Ball Lens (+/- 2 degrees) |

**Figure 5.9  Tolerance data as used by ZEMAX® to estimate the uncertainty in the bias estimate due to tilt of the aperture.**

5.3.5.  Ball Lens Misalignment

When the ball lens is randomly repositiond, the center of the ball may not fall on the center line through the aperture.  This is equivilant to a lateral misalignment of the ball lens with respect to the aperture.  We have assumed that this misslignment is zero on average.  Lateral misalignment of the ball lens with respect to the aperture will manifest itself as tilt in the wavefront.  It will also contribute to higher order aberrations since the ball lens/aperture system is no longer symmetric.  The unceartainty in the mean value of the misalignment contributes to the unceartainty on the bias estimate.

The sensitivity coefficiants were estimated using ZEMAX®.  First, the inverse tolerance feature was used to determine the lateral displacement required to produce the range of tilt coefficients observed in the measured data.  It is difficult to separate the effects of tilt about the x-axis and tilt about the y-axis.  Therefore, the root sum square of the tilt coefficients is used as a measure of tilt.  The sensitivity of each Zernike coefficient to lateral displacement of the ball lens, as measured by this combined tilt term, is the ratio of the standard deviation of the combined tilt term to the standard deviation of the  Zernike coefficient.  The sensitivity coefficient is assumed to be a constant for each Zernike coefficient over the range of interest.  This is similar to the technique used to in section 5.3.3 to calculate the sensitivity coefficient for misalignment of the aperture.  The standard uncertainty in the misalignment  is the standard deviation of the combined tilt term divided by the square root of the number of samples.  It is assumed that these misalignments  will  be  normally  distributed  within  the  tolerance  range  given  in  the calibration procedure.

### 5.3.6.  NA Mismatch

As discussed at the beginning of this chapter, we used a simple approximation of the sensitivity of a shearing interferometer to choose the numerical aperture of the ball lens/ aperture system used for the calibration.  The actual uncertainty in the bias estimate due to NA mismatch is dependent on the magnitude and radial order of the aberration. However,  as discussed in at the beginning of this chapter, the worst case uncertainty of the bias estimate will be 1% of the coefficient's value.    This is the value used as the sensitivity coefficient.  It is multiplied by the bias estimate to compute the contribution of the NA mismatch to  the combined uncertainty in the bias estimate.

CHAPTER 6: CONCLUSIONS AND RECOMMENDATIONS

The interferometer bias for each Zernike coefficients along with the associated combined standard uncertainties and expanded uncertainties are stated in table 6.1. Given the consistently large number of effective degrees of freedom, the expanded uncertainties were calculated using a coverage factor of k=2.0 for a confidence interval of 95.45%. A phase map of the bias and an uncertainty map calculated from equation 4.7 are shown in figure 6.1. The average repeatability of the measurement within a sample and the reproducibility of the measurement between calibration runs is included in the table for comparison.

The uncertainties in the bias estimate for the lower order Zernike terms is on the order of several hundredths of a wave. This is a significant proportion of the tolerance for many applications (see Chapter 1). The dominant contributor to the uncertainty for many of the coefficients was the lateral misalignment of the ball lens with respect to the aperture as measured by the variation of the x and y tilt coefficients within each calibration run. This was most likely due to the poor quality of the indentation used to center the ball lens onto the aperture. A more repeatable fixture might be fabricated by turning a cone in a metal blank and grinding the back side until an aperture of the appropriate size is created (see figure 6.2). A three point kinematic mount would be ideal, however, it is not clear how the aperture would be defined.

**Table 6.1 Results of the calibration.**

**units are in waves at a wavelength of 632.8 nm**

| Term Number | Bias Estimate | Combined Uncertainty (U_c) | Expanded Uncertainty (U_{95.45}) | Measurement Repeatability | Reproducibility Between Calibration Runs |
|---|---|---|---|---|---|
| 1 | -0.0781 | 0.0883 | 0.1766 | 0.0009 | 0.0011 |
| 2 | -0.0875 | 0.1028 | 0.2057 | 0.2980 | 0.2433 |
| 3 | 0.0982 | 0.1038 | 0.2076 | 0.3153 | 0.3567 |
| 4 | -0.0895 | 0.0779 | 0.1558 | 0.0310 | 0.0327 |
| 5 | -0.4126 | 0.0779 | 0.1558 | 0.0180 | 0.0220 |
| 6 | 0.2489 | 0.0853 | 0.1706 | 0.0102 | 0.0067 |
| 7 | 0.0058 | 0.0509 | 0.1018 | 0.0107 | 0.0103 |
| 8 | -0.0005 | 0.0375 | 0.0750 | 0.0124 | 0.0113 |
| 9 | -0.0563 | 0.0069 | 0.0138 | 0.0093 | 0.0105 |
| 10 | 0.0844 | 0.0116 | 0.0233 | 0.0249 | 0.0315 |
| 11 | -0.0938 | 0.0189 | 0.0377 | 0.0171 | 0.0130 |
| 12 | 0.0330 | 0.0091 | 0.0183 | 0.0113 | 0.0125 |
| 13 | 0.0072 | 0.0110 | 0.0220 | 0.0071 | 0.0069 |
| 14 | -0.0159 | 0.0072 | 0.0144 | 0.0253 | 0.0340 |
| 15 | 0.0177 | 0.0066 | 0.0132 | 0.0065 | 0.0059 |
| 16 | 0.0050 | 0.0033 | 0.0067 | 0.0076 | 0.0062 |
| 17 | 0.0024 | 0.0092 | 0.0185 | 0.0272 | 0.0322 |
| 18 | 0.0670 | 0.0217 | 0.0434 | 0.0190 | 0.0227 |
| 19 | -0.0301 | 0.0059 | 0.0118 | 0.0166 | 0.0201 |
| 20 | -0.0268 | 0.0099 | 0.0198 | 0.0091 | 0.0120 |
| 21 | 0.0196 | 0.0047 | 0.0095 | 0.0120 | 0.0147 |
| 22 | 0.0007 | 0.0057 | 0.0115 | 0.0079 | 0.0056 |
| 23 | -0.0157 | 0.0050 | 0.0100 | 0.0103 | 0.0139 |
| 24 | -0.0003 | 0.0045 | 0.0090 | 0.0105 | 0.0119 |
| 25 | -0.0049 | 0.0038 | 0.0075 | 0.0041 | 0.0001 |
| 26 | 0.0061 | 0.0122 | 0.0243 | 0.0180 | 0.0144 |
| 27 | -0.0517 | 0.0198 | 0.0396 | 0.0170 | 0.0184 |
| 28 | 0.0188 | 0.0061 | 0.0123 | 0.0167 | 0.0214 |
| 29 | 0.0305 | 0.0084 | 0.0169 | 0.0137 | 0.0184 |
| 30 | -0.0146 | 0.0054 | 0.0108 | 0.0091 | 0.0129 |
| 31 | -0.0092 | 0.0054 | 0.0108 | 0.0068 | 0.0046 |
| 32 | 0.0065 | 0.0063 | 0.0125 | 0.0076 | 0.0059 |
| 33 | -0.0031 | 0.0046 | 0.0092 | 0.0049 | 0.0044 |
| 34 | -0.0020 | 0.0062 | 0.0124 | 0.0075 | 0.0087 |
| 35 | -0.0004 | 0.0042 | 0.0084 | 0.0095 | 0.0087 |
| 36 | -0.0081 | 0.0031 | 0.0062 | 0.0057 | 0.0070 |
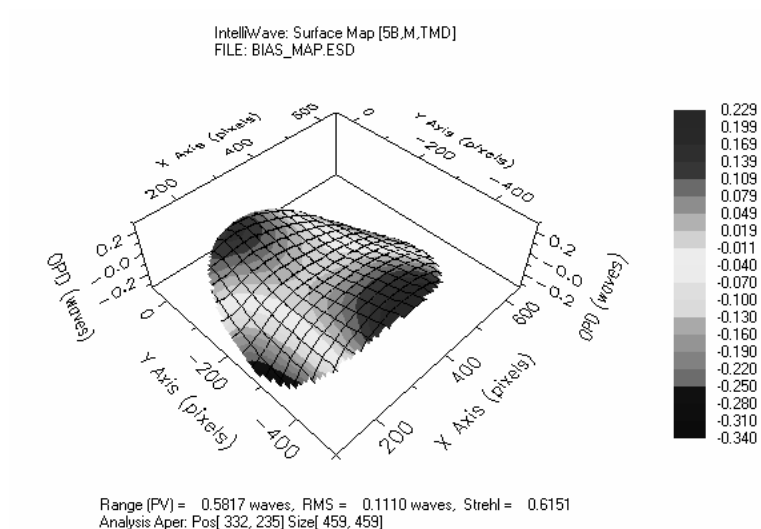
**(a)**
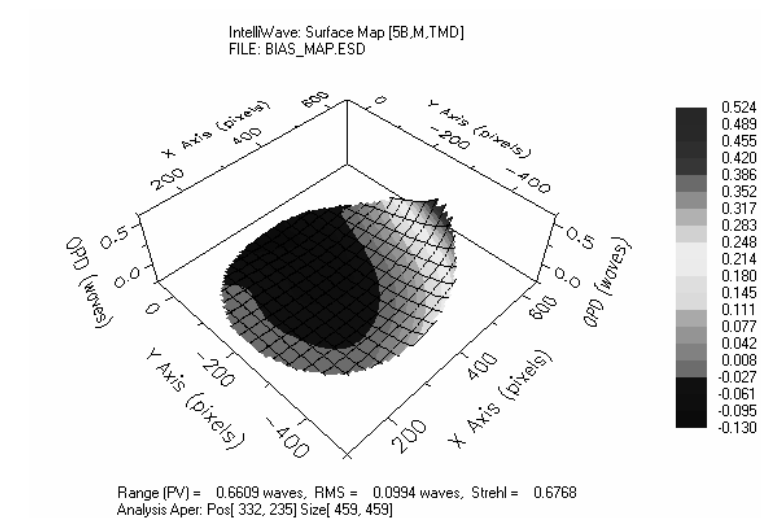


**(b)**

**Figure 6.1  Phase maps of the (a) bias estimate and (b) the expanded uncertainty in the bias estimate.**
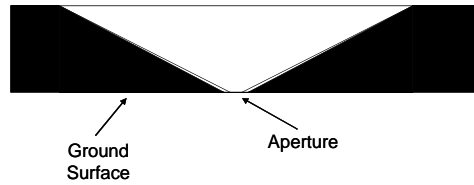
**Figure 6.2 Cross section of proposed mount with integrated aperture to reduce the uncertainty do to the ball lens misalignment.**

Astigmatism (term 5 and term 6) appears to be the dominant aberration contributing to the system bias. This agrees with a previous calibration of a different interferometer using the same technique and the same reference objective.[55]

We have extended the averaging technique for self-calibration to determine the systematic bias of a Mach-Zehnder interferometer used to measure the transmitted wavefront error for micro-refractive lenses. This technique should be compared with the results obtained by calculating the transmitted wavefront error from accurate form measurements or other calibration techniques. It may also be applied to other test configurations for measuring transmitted wavefront such as double pass Twyman-Green, Hartman tests and shearing interferometers described in chapter 2. Finally, this technique could be extended to configurations used to measure systems of micro-optics including both passive and active components.

REFERENCES

1.  K. Iga, Y. Kokubun, and M. Oikawa, Fundamentals of Microoptics, (Academic Press, Orlando, 1984), p. 1.

2.  J. Jahns, "Planar integrated free space optics," in Micro-optics, H.P. Herzig ed., (Taylor and Francis, Philadelphia, 1997), p. 180.

3.  W. Singer and K.H. Brenner, "Stacked micro-optical systems," in Micro-optics, H.P. Herzig ed., (Taylor and Francis, Philadelphia, 1997), pp. 214-216.

4.  M. Testorf and J. Jahns, "Imaging properties of planer integrated micro-optics," *JOSA A* **16**, 1175-1183 (1999).

5.  W.J. Smith, Modern Optical Engineering 2$^{nd}$ ed., (McGraw-Hill, New York, 1990), pp. 336-339.

6.  R.E. Wagner and W.J. Tomlinson, "Coupling efficiency of optics in single-mode fiber components," *Appl. Opt.*. **21**, 2671-2688 (1982).

7.  F. Welsh, "Global perspectives on optoelectronics industry," presented at the University of North Carolina Center for Optoelectronics and Optical Communications First Annual Symposium, Charlotte, NC (2002).

8.  D.C. O'Shea, T.J. Suleski, A. D. Kathman, and D.W. Prather, Diffractive Optics: Design, Fabrication, and Test, (SPIE Press, Bellingham, WA, 2004), p. 15.

9.  G. R. Brady, Master's thesis, McGill University, Montréal (2000).

10. M. A. Davies, C. J. Evans, S. R. Patterson, R.R. Vohra, and B. C. Bergner, "Applications of precision diamond machining to the manufacture of microphotonic components," *Proc. SPIE* **5183**, 94-108 (2003).

11. M.T. Gale, "Replication," in Micro-optics, H.P. Herzig ed., (Taylor and Francis, Philadelphia, 1997), pp. 153-177.

12. K. Mersereau, R.J. Crisci, C.R. Nijander, W.P. Townsend, D. Daly, and M.C. Hutley, " Testing and measurement of mircolenses." *Proc. SPIE* **1992**, 210-215 (1993).

13. L.A. Selburg, "Radius measurement by interferometery," *Opt. Eng.* **31**, 1961-1966 (1992).

14. M. Born and E. Wolf, Principles of Optics, 7$^{th}$ ed., (Cambridge University Press, Cambridge, 1999), pp. 543-547.

15.    A. Davies, B. Bergner, N. Gardner, "Improving metrology for micro-optics manufacturing," *Proc. SPIE* **5177**, 67-81 (2003).

16.    C.J. Evens, R.J. Hocken, and W. T. Estler, "Self-calibration: reversal, redundancy, error separation, and "absolute testing"," *CIRP Annals* **45**, 617-634 (1996).

17.    M. Raugh, "Two-dimensional stage self-calibration: Role of symmetry and invariant sets of points," *J. Vac. Sci. Technol. B.* **15**, 2139-2145 (1997).

18.    W.T. Estler, "Unceartainty analysis for angle calibrations using circle closure," *J. Res. Natl. Inst. Std. Technol.* **103**, 141-151 (1998).

19.    K. Creath and J.C. Wyant, "Absolute measurement of surface roughness," *Appl. Opt.* **29**, 3823-3827 (1990).

20.    H-J. von Martens, "Evaluation of uncertainty in measurements − problems and tools," *Optics and Lasers in Engineering* **38**, 185-206 (2002).

21.    P.R. Bevington and D.K. Robinson, <u>Data Reduction and Error Analysis for the Physical Sciences</u>, McGraw-Hill, Boston (2003), pp. 39-40.

22.    J. Mandel, <u>The Statistical Analysis of Experimental Data</u>, Dover, New York (1984), pp. 54-55.

23.    A.E. Jensen, "Absolute calibration method for laser Twyman-Green wave-front testing interferometers," *J. Opt. Soc. Am.* **63**, 1313 (1973).

24.    B.S. Fritz, "Absolute calibration of an optical flat," *Opt. Eng.* **23**, 379-383 (1984).

25.    C.J. Evans and R.N. Kestner, "Test optic error removal," *Appl. Opt.* **35**, 1015-1021 (1996).

26.    R.E. Parks, C. Evens, and L. Shao, "Calibration of interferometer transmission spheres," poster presented at Optical Fabrication and Testing, Kona, Hawaii (1998).

27.    N. Gardner, T. Randolph, A. Davies, "Self-calibration for micro-refractive lens measurements," *Proc. SPIE* **5180**, 244-252 (2003).

28.    D. Malacara, "Tyman-Green Interferometer," in <u>Optical Shop Testing,</u> 2nd ed., D. Malacara ed., (John Wiley & Sons, New York, 1992), pp. 68-69.

29.    J. Dyson, "Unit magnification optical system without Seidel aberrations," *J. Opt. Soc. Am.* **49**, 713-716 (1959).

30. M. Bray, "Stitching Interferometery: Side effects and PSD," *Proc. SPIE* **3782**, 443-452 (1999).

31. P.D. Pulaski, J.P. Roller, D.R. Neal, K. Ratte, "Measurement of aberrations of microlenses using a Shack-Hartmann wavefront sensor," *Proc. SPIE* **4767**, 44-52 (2002).

32. H. Schreiber, L. Lindlein, and J. Schwider, "A lateral shearing setup for testing microlenses in the near infrared region," *EOS Topical Meeting* **2**, 65-69 (1997).

33. N. Lindlein, H. Shriber, J. Schwider, and H. Sickinger, "The measurement of microlens parameters using shearing interferometer," *EOS Topical Meeting* **2**, 55-64 (1993).

34. H. Sickinger, O. Falkenstörfer, N. Lindein, and J. Schwider, "Charicterization of microlenses using phase a phase-shifting shearing interferometer," *Opt. Eng.* **33**, 2680-2686 (1994).

35. P.H. Malyak, D.L. Kent, P. Kolodner, J. Crawford, "Interferometric measurement of the back focal length and insertion loss of precision microlens arrays," *Proc. SPIE* **4437**, 161-171 (2001).

36. M. Testorf and S. Sinzinger, "Evaluation of microlens properties in the presence of high spherical aberration," *Appl. Opt.* **34**, 6431-6437 (1995).

37. M.C. Hutley, D. Daly, and R.F. Stevens, "The testing of microlens arrays," *IOP Short Meetings* **30**, 67-81 (1991).

38. L. Hale, E. Motamedi, and W, Gunning, "Optical testing of microlens arrays," *Proc. SPIE* **1751**, 47-51 (1992).

39. D. Daly and M.C Hutley, "Mircrolens measurements at NPL," EOS Topical Meeting **2**, 50-54 (1993).

40. P. Hariharan, <u>Basics of Interferometry</u>, (Academic Press, Boston, 1992), pp. 8-10.

41. A. Dandridge and A.B. Tveten, "Phase compensation in interferometeric fiber-optic sensors," *Opt. Lett.* **7**, 279-281(1982).

42. D.A. Jackson, R. Priest, A Dandridge, and A.B. Tveten, "Elimination of drift in single-mode optical fiber interferometer using a piezoelectrically stretched coiled fiber," *Appl. Opt.* **19**, 2926-2929 (1980).

43. J. Schwider and O. Falkenstörfer, "Twyman-Green interferometer for testing microspheres," *Opt. Eng.* **34**. 2972-2975 (1995).

44. D.S. Goodman, "Basic optical instruments," in <u>Geometrical and Instrumental Optics</u>, D. Malacara ed., (Academic Press, Boston, 1988), pp. 132-142.

45. W.J. Smith, <u>Modern Optical Engineering</u> 2<sup>nd</sup> ed., (McGraw-Hill, New York, 1990), pp. 142-143.

46. Intelliwave™ manual (Engineering Synthesis Design, Tucson, AZ, 2002).

47. ZEMAX® Users Guide (Focus Software, Inc., Tucson, AZ, 2001).

48. D. Malacara and S.L. DeVore , "Interferogram analysis and wavefront fitting," in <u>Optical Shop Testing,</u> 2<sup>nd</sup> ed., D. Malacara ed., (John Wiley & Sons, New York, 1992), pp. 464-466.

49. D. Malacara, "Mathematical Interpretation of Radial Shearing Interferometers," *Appl.Opt*., **13**, 1781-1784 ,1974

50. D. Malacara, "Radial, rotational, and reversal shear interferometers," in <u>Optical Shop Testing</u>, 2<sup>nd</sup> ed.,  D. MAlacara ed., (John Wiley & Sons, New York, 1992), pp. 173-177.

51. N. Gardner, Master's thesis, University of North Carolina at Charlotte, Charlotte, NC (2003).

52. J. Mandel, <u>The Statistical Analysis of Experimental Data</u>, Dover, New York (1984), p. 59.

53. E. Dietrich and A. Schulze, <u>Statistical Procedures for Machine and Process Qualification</u>, (ASQ Quality Press, Milwaukee,  Wisconsin, 1999), pp. 301-307.

54. B.N. Taylor and C.E. Kuyatt, Guidelines for Evaluating and Expressing the Uncertainty if NIST Measurement Results, NIST Technical Note 1297, US Government Printing Office, Washington D.C (1994)

55. B. Bergner and A. Davies, "Self-calibration technique for transmitted wavefront measurements," *Proc. SPIE* **5180**, 239-243 (2004).

APENDIX A:  CALIBRATION PROCEDURE

The following procedure was used to calibrate the interferometer.  It assumes that the interferometer has been aligned and is in the Mach-Zehnder configuration.  It also assumes that the phase shift has been calibrated.  For further detail on using Inteliwave™ and Zemax® see references 44 and 45.

1. Select a reference objective.  It should have a numerical aperture larger than, but approximately equal to, the numerical aperture of the lenses that will be tested. The focal length should be chosen so that the exit pupil of the lens under test can be imaged onto the detector as described in section 3.2.  (Alternate objective and imaging lens combinations can be evaluated using a simple spread sheet.)

2. Select a ball lens and pin-hole aperture with a numerical aperture approximately equal to the numerical aperture of the test lens as discussed in section 4.2.  (The solve feature in ZEMAX® can be used to quickly evaluate ball lens/aperture systems designed from commercially available components).

3. Place the ball lens in the center of the pin hole aperture.  Alignment of the ball lens may be aided by slightly indenting the center of the pin hole aperture.  Place the ball lens/aperture system into the interferometer in place of the lens under test. It may be necessary to place spacers under the assembly so that the ball lens is confocal with the reference objective when the axial adjustment of the lens mount is in its center of travel.

4. Visually align the face of the aperture perpendicular to the optical axis of the interferometer using the tip/tilt adjustments on the microscope stage.

5.  Align the ball lens/aperture in the interferometer. Focus the imaging system on the exit pupil of the lens. Two to three tilt fringes may aid in determining best focus. The edge of the aperture will appear as several thin lines that will converge as the aperture is brought into focus.

6.  Create or load an appropriate software mask. The mask should follow the image of the aperture. The mask may be elliptical depending on the aspect ration of the camera and the setting sin Inteliwave™. During the analysis Inteliwave™ will normalize the data in inside the mask to a unit circle before fitting the Zernike polynomials.

7.  Set the number of measurements to average to 10.

8.  Take several measurements, moving the ball lens/aperture laterally and axially to minimize the Xtilt, Ytilt, and Power terms in the Zernike polynomial. (Each term should be less than 0.2 waves).

9.  Take a measurement and export the Zernike coefficients to a spreadsheet.

10. Randomly reposition the ball lens in the aperture with a puff of air from a lens blower brush. Continue to blow on the lens until it settles back onto the aperture with less than three fringes of tilt.

11. Repeat steps 9 and 10 approximately fifty to seventy times. The contribution of the figure error of the ball lens and random noise will decrease in proportion to the inverse square root of the number of repetitions.